

CHES: an Innovative Concept for High-Resolution, Far-UV Spectroscopy

Instrument Design, Inception, and Results from the First Two Sounding Rocket Flights

Keri Hoadley · Kevin France · Nicholas
Nell · Robert Kane · Brian Fleming ·
Allison Youngblood · Matthew Beasley

Received: date / Accepted: date

Abstract The space ultraviolet (UV) is a critical astronomical observing window, where a multitude of atomic, ionic, and molecular signatures provide crucial insight into planetary, interstellar, stellar, intergalactic, and extragalactic objects. The next generation of large space telescopes require highly sensitive, moderate-to-high resolution UV spectrograph. However, sensitive observations in the UV are difficult, as UV optical performance and imaging efficiencies have lagged behind counterparts in the visible and infrared regimes. This has historically resulted in simple, low-bounce instruments to increase sensitivity. In this study, we present the design, fabrication, and calibration of a simple, high resolution, high throughput FUV spectrograph - the *Colorado High-resolution Echelle Stellar Spectrograph* (CHES). CHES is a sounding rocket payload to demonstrate the instrument design for the next-generation UV space telescopes. We present tests and results on the performance of several state-of-the-art diffraction grating and detector technologies for FUV astronomical applications that were flown aboard the first two iterations of CHES. The

Keri Hoadley
California Institute of Technology, Dept. of Physics, Mathematics, & Astronomy, Cahill
Center for Astronomy & Astrophysics, Pasadena, CA 91125, USA
David & Ellen Lee Postdoctoral Fellow in Experimental Physics at Caltech
University of Iowa, Dept. of Physics & Astronomy, Van Allen Hall, Iowa City, IA 52242 USA
E-mail: khoadley@caltech.edu

Kevin France · Nicholas Nell · Brian Fleming · Allison Youngblood
Laboratory for Atmospheric and Space Physics, University of Colorado, UCB 392, Boulder,
CO 80309, USA

Robert Kane
Blue Canyon Technologies, 2550 Crescent Drive, Lafayette, CO 80026, USA

Matthew Beasley
Southwest Research Institute, Department of Space Studies, 1050 Walnut Ave., Boulder,
CO, 80302, USA

CHESSE spectrograph was used to study the atomic-to-molecular transitions within translucent cloud regions in the interstellar medium (ISM) through absorption spectroscopy. The first two flights looked at the sightlines towards α Virgo and ϵ Persei and flight results are presented.

Keywords Instrumentation: spectrographs - ISM: abundances, clouds, molecules - stars: individual (ϵ Per (HD 24760))

1 Introduction

Ultraviolet (UV) observations are critical for addressing a many key questions in nearly all aspects of astrophysics. UV observations probe the flow of energetics in the universe as UV photons affect atoms, molecules, ions, and dust. The UV is the peak of the hot star spectral energy distribution (SED), making it the ideal probe of massive (recent) star-formation and galactic star formation histories (e.g., Martin et al. 2005). A multitude of atomic, ionic, and molecular species have strong resonances with UV radiation, which pump and produce strong emission and absorption lines seen against the UV background. The UV is home to emission lines in collisional ionization equilibrium at formation temperatures up to $\sim 3 \times 10^5$ K (Tumlinson et al., 2017), critical for assessing hot interstellar, circumgalactic, and intergalactic environments. The only other wavelength regime with the potential to observe so many phases of gas and dust simultaneously is the far-IR, which similarly requires access to space. In cooler regimes of the interstellar medium (ISM), dust scatters and absorbs far-UV (FUV) photons, which provides a UV background that changes the chemistry of galactic ISMs (e.g., Hamden et al. 2013). While dust is often seen as a hindrance to UV observations, such sightlines can be used to sensitively measure fine dust chemistry and distributions in different astrophysical environments (e.g., Blasberger et al. 2017; Ma et al. 2020). Similarly, UV spectroscopy of relatively high reddening ($E(B-V) > 0.5$) sightlines have routinely been observed from space since the 1970s, with the *International Ultraviolet Explorer (IUE)* and Copernicus revolutionizing our understanding of the diffuse and translucent ISM physical state and chemistry using UV absorption line spectroscopy (e.g., Spitzer et al. 1973; Morton 1975; Savage et al. 1977; Bohlin et al. 1983, and many others). The UV is the only wavelength regime we gain access to cold molecular hydrogen (H_2 ; $T(H_2) < 500$ K), and this in itself is a critical diagnostic for many astrophysical environments and properties that rely on accurate measures of H_2 density or mass. UV observations provide a critical look at the characteristics of many astrophysical systems, both nearby and afar.

Present-day ultraviolet spectroscopic facilities on community space telescopes (currently, only the *Hubble Space Telescope (HST)* Cosmic Origins Spectrograph (COS; Green et al. 2012) and Space Telescope Imaging Spectrograph (STIS; Kimble et al. 1998) provide spectroscopic coverage in the FUV) have provided a unique view of many astrophysical systems, but they have their limitations and cannot address all our remaining questions. Current space facility

spectrographs rely on old technologies in reflective mirror coatings, gratings, and detectors that all perform moderately in the UV - many gains in improvement can be made in almost all realms of UV instrumentation to probe deeper and fainter objects in our universe. Many of the most interesting, intriguing, and mysterious diffuse objects discovered by the *Galaxy Evolution Explorer* (*GALEX*) a decade ago (e.g., Martin et al. 2007; Sahai & Chronopoulos 2010; Hoadley et al. 2020) are unattainable with UV spectrographs on *HST*, which do not have the sensitivity to observe them. Highly sensitive, high-resolution UV spectroscopy is necessary to address astronomical questions that are beyond the reach of present-day instruments. In this paper, we discuss a concept for a high-throughput, high-resolution ($R > 100,000$) far-UV (1000 - 1600 Å) spectrograph to serve as an instrument baseline for the next generation of UV-Visible space telescopes (e.g, France et al. 2016a; Woodruff et al. 2019; The LUVVOIR Team 2019).

1.1 Instrument Overview

The *Colorado High-resolution Echelle Stellar Spectrograph* (CHES) is an objective echelle spectrograph designed to achieve a minimum resolving power (R) $> 100,000$ through the far-UV (1000 – 1600 Å) (Hoadley et al., 2016, 2014; France et al., 2012; Kane et al., 2011; Beasley et al., 2010; France et al., 2016b). CHES does not utilize a telescope, but rather light is fed into the spectrograph through a collimator. In this way, the instrument consists of a 2-bounce system, minimizing the number of reflections required of the far-UV photons before being captured by the detector. The focusing optic of the system is tied into the cross-dispersing grating, which also includes additional surface curvature orthogonal to the focusing axis to correct for first-order aberrations in the spectral line.

CHES demonstrates an innovative high-resolution FUV spectrograph design, ideal as an ancillary instrument for future space telescopes. The instrument also serves as a platform to test, verify, and flight-qualify the performance of both grating and detector technologies for UV astrophysical applications. Highly sensitive instruments for future missions will require high efficiency and low scattered light and background levels, which are of the highest priority to address for the UV instrumentation community (e.g. Scowen et al. 2017 and references therein). All optical (echelle and cross-dispersing gratings) and detector (cross-strip anode microchannel plate (MCP)) components on CHES were experimental, with technology readiness levels (TRLs) ≤ 6 .

CHES is a rocket-borne astronomical instrument that has launched on four separate NASA-funded sounding rocket missions. We report on the design, build, calibration, and integration leading to the first two flights of CHES. We present the observations from both launches, and an in-depth analysis of the sightline observed on the second flight.

1.2 Scientific Program

The FUV bandpass and high spectral resolution of CHESS are ideally suited to study interstellar structures in the sightlines of hot, massive O- and B-type stars.

Translucent clouds reside in the transition between the diffuse (traditionally defined as the visual dust extinction ($A_V < 1$) and dense ($A_V > 3$) phases of the interstellar medium (ISM). It is in this regime where the UV portion of the average interstellar radiation field plays a critical role in the photochemistry of the gas and dust clouds that pervade the Milky Way galaxy. One powerful technique for probing the chemical structure of translucent clouds is to combine measurements of H_2 with knowledge of the full carbon inventory (CI, CII, and carbon monoxide (CO)) along a given line of sight. Snow & McCall (2006) argue that an analysis of the carbon budget should be the defining criterion for translucent clouds, rather than simple measurements of visual extinction. Moderate resolution 1000-1120 Å spectra from FUSE and higher-resolution spectra from HST/STIS can confirm whether or not a sightline is consistent with the existence of translucent material in the framework of current models of photodissociation regions of the ISM ($CO/H_2 > 10^{-6}$ and $CO/CI \sim 1$; Burgh et al. 2007, 2010).

The bandpass of CHESS contains absorption lines of H_2 (1000 – 1120 Å), CII (1036 and 1335 Å), CI (1103 – 1130, 1261, 1561 Å), and several bands of CO (< 1510 Å). High resolution ($R > 100,000$) is required to resolve the velocity structure of both the CI lines and the rotational structure of CO, essential to accurately determine the column density of these species (Jenkins & Tripp, 2001). The FUV bandpass also provides access to many ionic absorption lines to explore the depletion patterns of metals in translucent clouds.

The Local Interstellar Medium (LISM) provides an opportunity to study general ISM phenomena up close and in three dimensions, including interactions of different phases of the ISM, cloud collisions, cloud evolution, ionization structure, thermal balance, and turbulent motions (Redfield, 2006). Our immediate interstellar environment also determines the structure of the heliosphere, or the momentum balance of the solar wind and the surrounding ISM. Several physical characteristics of the LISM are measurable, including the ionization structure. Since many clouds in the LISM are optically thin, the distribution of ionizing sources (i.e., hot stars) determines the three-dimensional ionization structure of the LISM.

Measurements of different ionization species are required to probe different phases of the LISM. In addition to local ionization structure, temperature and elemental depletion structure are also critical to understanding the three-dimensional morphology of the LISM. The temperature distribution of the LISM can place constraints on models of the evolution of the local solar neighborhood. Determining these temperatures requires high spectral resolution so that contributions from thermal and turbulent motions can be distinguished, a capability that is achievable with CHESS.

2 Instrument Concept

CHES is an objective $f/12.4$ echelle spectrograph. The instrument design included the development of two novel grating technologies and flight-testing of a cross-strip anode microchannel plate (MCP) detector (Beasley et al., 2010). The high-resolution instrument is capable of achieving resolving powers $\geq 100,000 \lambda/\Delta\lambda$ across a bandpass of $1000 - 1600 \text{ \AA}$ (Hoadley et al., 2014; France et al., 2016b).

2.1 Spectrograph Design

The optical design of CHES is as follows:

- A mechanical collimator, consisting of an array of $10.74 \text{ mm} \times 10.74 \text{ mm} \times 1000 \text{ mm}$ anodized aluminum tubes, provides CHES with a total collecting area of 40 cm^2 , a field of view (FOV) of 0.67° , and allows on-axis stellar light through to the spectrograph. A mechanical collimator design was chosen over a traditional telescope design for practicality, while still achieving the necessary sensitivity for the spectrograph. A collimating telescope would be difficult to align to the spectrograph and remain aligned during the course of its flight. A wire mesh collimator was considered, but the total loss of collecting area was too high to implement. The large FOV of the mechanical collimator was dictated by the physical dimensions of commercially-available anodized aluminum tubes. Because CHES looks at bright FUV point sources (stars) to provide a “backlight which illuminates the interstellar gas in the sightline, there was very little chance of source confusion over this FOV, given the effective area of the spectrograph and the brightness of the target stars.
- A square echelle grating (ruled area: $100 \text{ mm} \times 100 \text{ mm}$), with a designed groove density of 69 grooves/mm and angle of incidence (AOI) of 67° , intercepts and disperses the FUV stellar light into higher diffraction terms ($m = 266 - 166$). The custom echelle was used to research new etching technologies, namely the electron-beam (e-beam) etching process. The results of the JPL fabrication effort are discussed in Section 2.2.1.
- Instead of using an off-axis parabolic cross disperser (Jenkins et al., 1988), CHES employs a holographically-ruled cross dispersing grating with a toroidal surface figure and ion-etched grooves, maximizing first-order efficiency. The cross disperser is ruled over a square area ($100 \text{ mm} \times 100 \text{ mm}$) with a groove density of 351 grooves/mm and has a surface radius of curvature (RC) = 2500.25 mm and a rotation curvature (ρ) = 2467.96 mm . The grating spectrally disperses the echelle orders and corrects for grating aberrations (Thomas, 2003).
- The cross-strip MCP detector (Vallerga et al., 2010; Siegmund et al., 2009) is circular in format, 40 mm in diameter, and capable of total global count rates $\sim 10^6 \text{ counts/second}$. The cross-strip anode allows for high resolution imaging, with the location of a photoelectron cloud determined by the

centroid of current read out from five anode “fingers” along the x and y axes.

Because the echelle disperses light into high orders and the cross disperser separates light sharing the same echelle diffraction order solutions, the final data product is a series of spectra, where each echelle spectrum provides a small fraction of the total spectral coverage of the instrument. At the same time, each spectral snippet in the full raw data is able to be sampled at high resolution. This is how CHESS is able to achieve both large wavelength coverage and high resolution.

The CHESS instrument also includes an optical system (Xybion Model ISS-255 low-light video camera¹), which was used to align the spectrograph to an independent star tracking system during calibrations and flight. The aspect camera relies on the positions of the instrument gratings to direct zeroth-order light to a visible-light camera. Fig. 1 shows a Zemax ray trace of collimated (star) light through the entire spectrograph.

CHESS was separated into two sections to fly aboard a sounding rocket mission: a vacuum (spectrograph) and non-vacuum (electronics) section. The two sections are separated by a hermetic bulkhead. The detector was mounted with a hermetic seal on the electronics side of the vacuum bulkhead, facing into the spectrograph section. The overall length of the payload was 226.70 cm from mating surface to mating surface, with a total weight of about 365 lbs. The opto-mechanical design of the spectrograph consisted of a carbon-fiber space frame attached to the vacuum side of the hermetic bulkhead. The carbon fiber frame (five 2.54 cm diameter x 182.88 cm long tubes) holds three light-weighted aluminum disks which suspend the mechanical collimator, echelle grating and cross-disperser in place. The aspect camera is attached to the vacuum side of the hermetic bulkhead. A Solidworks rendering of the payload is shown in Figure 2.

2.2 Components & Performance

The CHESS instrument is comprised of three optical components: two gratings (one high-dispersion echelle grating and one cross-dispersing grating) and one detector (cross-strip anode MCP). Table 1 presents technical details about each optical element used for the first two flights of the instrument.

2.2.1 Echelle Grating Development for FUV Applications

Echelle gratings are distinguishable by their low line densities (20 - 300 lines/mm) and use at steep facet angles (θ : 20° - 80°). Both qualities allow echelle gratings

¹ At the time of CHESS-1 and 2, the Xybion Electronics System (XES) low-light camera was deprecated and the NASA Sounding Rocket Operations Contract (NSROC) was in the process of replacing it with a newer model of space-qualified low-light camera system. In 2018, NSROC officially replaced the XES Model ISS-255 with the Stanford Photonics Inc. XR/M model: <https://www.stanfordphotonics.com/Products/products.htm>

Table 1 Instrument Specifications for the CHESS Sounding Rocket Payload

Mechanical Collimator		Spectrograph	
FOV: 18.5' × 18.5'		Bandpass (Å): 1000 - 1650	
Dimensions (mm): 10.74 × 10.74 × 1000		Resolving power: Theoretical R ~ 120,000 Demonstrated R ≤ 10,000	
Collecting area (cm ²): 40.0		$F\#$: $f/12.4$	
Echelle (CHESS-1)	Echelle (CHESS-2)	Cross Disperser	Detector
Vendor: LightSmyth	Vendor: Bach Research	Vendor: HORIBA Jobin-Yvon	Vendor: Sensor Sciences
Shape: Flat	Shape: Flat	Shape: Toroidal	Type: Open-face MCP
Blaze angle(°): 73.0	Blaze angle(°): 64.3	Radius (mm): 2500.25/2467.96	Pixel format: 8k × 8k
Groove density (gr/mm): 71.7	Groove density (gr/mm): 53.85	Groove density (gr/mm): 351	Spatial resolution (μm): 25
Ruling: Lithographic	Ruling: Mechanical	Ruling: Holographic	Anode: Cross-strip
Coating: Al+LiF	Coating: Al+LiF	Coating: Al+LiF	Photocathode: CsI
Dimensions (mm): 100 × 100 × 0.7	Dimensions (mm): 104 × 104 × 16	Dimensions (mm): 100 × 100 × 30	Outer dimension (mm): 40
Material: Silicon	Material: Zerodur	Material: Fused Silica	Global count rate (Hz): 10 ⁶

to theoretically achieve high dispersion, high efficiency at or near the Littrow configuration, or where the angle of incidence equals the diffraction angle ($\alpha = \beta = \theta$), and high resolution with low polarization effects.

As a part of the instrument design, the echelle was meant to be an experimental technology demonstration piece for two different grating fabrication processes: the first was a lithographic-ruling process, provided by LightSmyth, Inc., and the second an electron-beam etching technique, fabricated by the Microdevices Laboratory at JPL. The lithographic ruling process starts with a substrate (silicon) with a thin oxidation layer, over which a photoresist and photomask with the desired groove pattern is overlaid. Using extreme-UV light to etch into the photoresist, the photomask is removed and the oxide layer is further etched via chemical agents that do not harm the photoresist. After removing the rest of the photoresist, the etched substrate is left with the desired groove density and thickness. The lithography process theoretically allows for the creation of uniform, low-scatter gratings at arbitrary groove densities with sub-100 nm surface deviations. The electron-beam etch scans a focused beam of electrons across the surface of the optic, which is covered with an electron sensitive film. The electron beam changes the solubility of the resist, which removes exposed regions of the resist in a solvent (McCord & Rooks, 2000). This technique also enables controlled line spacing on the grating and sub-10 nm surface deviations for low scatter grooves.

We present results from in-house determination of the groove efficiency of the best echelle gratings fabricated by both the lithography and electron-beam etching processes in Table 2 and Figure 3. The high angle of incidence and high diffraction orders we were working with in CHESS made the the fabrication process of the echelle gratings extremely difficult, and both manufacturers were unable to produce echelle gratings that met our flight specification

Table 2 Comparison of Echelle Performance for CHESS (Hoadley et al., 2016)

Grating	α (degrees)	Groove Density (grooves/mm)	Ly α Efficiency
CHESS, Designed	67.0	69.0	70.0 %
LightSmyth, CHESS-1	73.0	71.7	1.5 %
JPL Echelle	65.5	100.0	4.5 %
Bach, CHESS-2*	64.3	53.85	11.9 % + 8.4 %
Richardson*	63.0	87.0	62.0 %

in the limited time allowed before scheduled launches. For the first flight of CHESS, we had not identified a back-up grating to use for flight, so we flew the lithographically-ruled echelle. For CHESS-2, we identified two mechanical-ruling manufacturers that provided higher efficiency gratings for the second flight. The Bach echelle was delivered in time for the second flight, while the Richardson echelle was used for subsequent flights (Kruczek et al., 2017, 2018).

2.2.2 Cross-Dispersing Grating

The CHESS cross disperser grating is a 100 mm \times 100 mm \times 30 mm fused silica optic with a toroidal surface profile. The toroidal surface shape separates the foci of the tangential and sagittal axes of the dispersed light, which corrects astigmatic aberrations typically introduced by a more traditional off-axis parabolic design (e.g., Sasian 1997; Jenkins et al. 1996; Indebetouw et al. 2001). The surface figure of the toroid focuses the echelle order widths at the position as the spectral line widths, which are dictated by the grating solutions etched into the cross disperser. Both the sagittal and tangential foci of the toroidal optic do not intersect either the ion repeller or quantum efficiency (QE) grids, both of which are placed in front of the detector. The cross dispersing optic is a novel type of imaging grating that represents a new family of holographic solutions and was fabricated by Horiba Jobin-Yvon (JY). The line densities are low (351 lines per mm, difficult to achieve with the ion-etching process), and the holographic solution allows for more degrees of freedom than were previously available with off-axis parabolic cross dispersing optics. The holographic ruling corrects for aberrations that otherwise could not be corrected via mechanical ruling. The grating is developed under the formalism of toroidal variable line spacing (VLS) gratings (Thomas, 2003) and corresponds to a holographic grating produced with an aberrated wavefront via deformable mirror technology. This results in a radial change in groove density and a traditional surface of concentric hyperboloids from holography (e.g., HST/COS; Green et al. 2012).

Figure 4 shows the measured reflectivity (order efficiency times the reflectivity of the optical coating) of the cross dispersing optic for order $m = -1$, which is the dispersion order used in the CHESS instrument. We measure the reflectivity of the cross disperser before the launch of CHESS-1, between

the launch of CHESS-1 and CHESS-2, and after the launch of CHESS-2, and found that it did not change significantly over time. The cross disperser is effective at dispersing most of the on-axis light into the $m = \pm 1$ orders and suppressing the $m = 0$ order because of the characteristic sinusoidal groove profiles created via the ion-etching procedure. Additionally, at optical wavelengths, the reflectivity of the $m = 0$ order becomes comparable to the $m = \pm 1$ orders. This allowed us to build a secondary camera system to track the movements of our optical axis and target acquisition during flight.

2.2.3 Cross-Strip Microchannel Plate

The cross-strip MCP detector was built and optimized to meet the CHESS spectral resolution specifications at Sensor Sciences (Vallerga et al., 2010; Siegmund et al., 2009). The detector has a circular format and a diameter of 40 mm. The microchannel plates are lead silicate glass, containing an array of 10-micron diameter channels. They are coated with an opaque cesium iodide (CsI) photocathode, which provides $QE = 15 - 40\%$ at FUV wavelengths. When UV photons strike the photocathode to release photoelectrons, the photoelectrons are accelerated down the channels by an applied high voltage (~ 3100 V). Along the way, they collide with the walls of the channels, which produces a large gain over the initial single photoelectron. There are two MCPs arranged in a “chevron” configuration. During flight, the detector achieved spatial resolution (PSF) of $25 \mu\text{m}$ over an $8\text{k} \times 8\text{k}$ pixel format. The detector quantum efficiency (DQE) was measured by Sensor Sciences and is shown in Figure 5 (left).

2.2.4 Instrument Throughput and Effective Area

The designed throughput of CHESS was set assuming that certain milestones in grating etching processes, specifically higher efficiency, low scattered light echelle grating, were achieved. CHESS was designed as a 2-bounce spectrograph to minimize the total reflective surfaces and maximum throughput of the instrument. The specified echelle diffraction efficiency into Littrow orders through the CHESS bandpass was defined at 70%, a performance which matches echelle counterparts in visible and infrared spectrographs. The cross-strip MCP was coated with a photocathode to increase the DQE to $\sim 25\%$ average across the CHESS bandpass. The holographic ruling of the cross disperser has $\sim 50\%$ dispersion efficiency through the FUV. The reflective coating on both gratings is lithium fluoride over an aluminum layer (Al+LiF), which is $\sim 70\%$ reflective for $\lambda > 1050 \text{ \AA}$. This puts the total throughput of the designed CHESS instrument at $\sim 4.3\%$ average across the FUV bandpass. With a total collecting area of 40 cm^2 , the designed average effective area of CHESS was meant to be 1.75 cm^2 .

The component-level performance and total throughput of CHESS-1 and CHESS-2, defined as the effective area (the total throughput of the instrument $\times 40 \text{ cm}^2$ collecting area), are shown in Figure 5. The low effective area of the

instrument was driven by the efficiency of the echelle grating, which underperformed our specifications. The CHES-2 effective area improved by roughly an order of magnitude from CHES-1 by using a traditionally-ruled echelle grating, and subsequent flights of CHES have improved the throughput by continuing to exchange echelle gratings (Kruczek et al., 2017).

3 Pre-flight Calibrations & Data Reduction

Pre- and post-flight calibrations of CHES were performed in a dedicated vacuum chamber for sounding rocket payloads located in the Astrophysical Research Laboratory at the University of Colorado - Boulder. The chamber pumps the payload down to pressures of $< 10^{-5}$ Torr, allowing for UV light to transmit through the payload and safe operation of electronics requiring high voltage, such as the MCP detector. Because CHES was designed as a high-resolution spectrograph with a broad UV bandpass, a hollow-cathode arc lamp supplied with high purity H+Ar gas produced UV light used to focus and calibrate the instrument. This gas not only provided lines of hydrogen and argon, but a myriad of lines from H₂ fluorescence. Figure 6 shows the best-focused calibration images from CHES-1 and CHES-2 pre-flight spectra. The broadest emission features show atomic lines of hydrogen and argon, while the narrower features are H₂ fluorescence lines excited by interactions with energetic electrons within the lamp.

Calibration images like those shown in Figure 6 were used to convert the CHES echellogram to a 1-dimensional spectrum, defining both the wavelength solution and line spread function (LSF) of the instrument. First, each order dispersed by the cross disperser was identified and extracted to collapse into a 1D spectrum. Then, using adjacent order spectra, the orders were cross-correlated and stitched together to create a complete spectrum from 1000 - 1600 Å. The cross-correlation was a (roughly) linear function from orders with shorter wavelengths to longer wavelength orders, so adjacent orders with no overlapping features could still be co-added into the complete spectrum. A synthetic H₂ model of electron-impact fluorescence was used to match H₂ features in the CHES spectrum to the laboratory wavelengths of H₂ emission - this created the wavelength solution of the instrument, as shown in Figure 7.

Once a wavelength solution was found, we convolved each synthetic emission line with a Gaussian of unknown width to match the CHES emission line profiles, thereby creating LSF kernels through the CHES bandpass. Each line was best fit with a narrow and broad Gaussian component. Figure 8 shows a close-up of a few emission lines with a two-component Gaussian fit of the H₂ lines imaged by CHES.

The “broad” component of the CHES LSF was unexpected and severely impeded the spectral resolution of the instrument. CHES was designed with $R \geq 100,000$, but the measured resolution was $R \leq 8,000$. During the first build and calibration of CHES, it was thought that the experimental echelle

was the culprit of the degraded resolution, as it was etched onto a thin wafer that could bow or warp the surface of the grating.

It was determined during the calibration of CHESS-2 that the broad emission lines were the result of the cross dispersing grating - the toroidal shape of the optic was designed to focus and correct for optical aberrations, but the ruling of the grating occurred along the optical axis perpendicular to the radius of curvature, which meant that, while the order widths were minimized to avoid order confusion, the spectral lines were out-of-focus. We verified this was the culprit by flipping the grating axis of the cross disperser in our Zemax models, which perfectly reproduced the line shapes and measured spectral resolution of the instrument (Kruczek et al., 2018, 2019). While the cross disperser was never re-fabricated, Kruczek et al. 2018 addressed the spectral resolution issue by adding a slight curvature to the high-dispersion echelle grating, achieving $R \sim 14,000$ (Kruczek et al., 2019). However, for CHESS-1 and CHESS-2, the spectral resolution of the instrument remained at $R < 8,000$.

4 CHESS-1: α Virgo

The first flight of CHESS targeted the β Scorpii¹ (β Sco¹; HD 144217) sightline. β Sco¹ is spectroscopic binary comprised of a B0.5V and a B1.5V spectral type star at distance of 161 pc with intermediate reddening ($E(B-V) = 0.2$, $A_V \sim 0.6$; $\log N(\text{H}_2) \sim 19.8 \text{ cm}^{-2}$ (Savage et al., 1977)).

However, given the poor performance of the experimental echelle grating used in CHESS-1, the science team elected to define a back-up target to move to if the signal-to-noise (S/N) of β Sco¹ was insufficient to produce a science-quality spectrum during the limited time of the flight. The back-up target, α Virgo (α Vir; HD 116658; “Spica”), is a spectroscopic binary, consisting of a B1III-IV star + B2V star at a distance of 43 pc (Hoffleit & Jaschek, 1982), well within the Local Bubble ($E(B-V) = 0.03$, $A_V \sim 0.1$ Savage et al. 1977). α Vir outputs 4 – 5 times more far-UV flux than β Sco¹ and thus demonstrated the capabilities of the CHESS instrument.

CHESS-1 (NASA/CU mission 36.285 UG) was launched from White Sands Missile Range on 24 May 2014 at 01:35am using a two-stage Terrier/Black Brant IX vehicle. Data was downlinked through the NASA telemetry system in real-time as $[x, y, t, PHD]$ photon lists, where $[x, y]$ defines the digital pixel position of the photon recorded on the detector, t is the time the photon was recorded, and PHD is the pulse height recorded for the photon, which is related to detector gain. Overall, the mission was a comprehensive success and achieved all the goals it aimed to meet. The instrument successfully collected data over the allotted ~ 400 seconds of observing time. After the initial count rate on beta Sco was lower than expected, we elected to observe α Vir, and stayed on this target for the remainder of the flight. Count rate from α Vir was also lower than expected, but stellar absorption features in the echellogram made it clear that we were observing the star. Additionally, count rate contribution from air glow contamination was lower than expected, which suggested

that at least one of the optics became unaligned with the instrument between pre-flight operations and launch. Post-launch calibrations verified that one of the gratings shifted before flight – the echellogram did not appear on the detector until the instrument was shifted off-axis from the vacuum light source by ~ 1 degree.

Figure 9 shows the echellogram of α Vir from the CHESS-1 launch. Prominent features apparent in the echellogram include stellar Ly α , Si II (1193 Å), Si III (1206 Å), and C III (1175 Å). However, the S/N of the flight data were not adequate to reconstruct an analysis-quality 1D spectrum.

5 CHESS-2: ϵ Persei

CHESS-2 was launched aboard a Terrier-Black Brant IX sounding rocket from White Sands Missile Range on 21 February 2016 as a part of NASA/CU mission 36.297 UG. CHESS-2 observed the line of sight to ϵ Persei (ϵ Per; HD 24760). ϵ Per is a B0.5III star at $d \approx 300$ pc with low–intermediate reddening ($E(B-V) = 0.1$; $\log(H_2) \sim 19.5$), indicating that the sightline may be sampling cool interstellar material. H₂, C I, CO, and C II were all detected by Copernicus; however, higher sensitivity and spectral resolution is required for a complete analysis of these types of sightlines (Federman et al., 1980). Observations by Copernicus and IUE have been used to measure the velocity structure along the sightline to ϵ Per, and have found at least three separate cloud structures described by different kinematic behavior and molecular abundances (Bohlin et al., 1983). Resolving the various molecular clouds on the ϵ Per sightline is the primary goal of CHESS-2. Overall, the line of sight to ϵ Per shows typical abundances of molecular material and ionized metal found in translucent clouds, such as H₂, Fe II and Mg II (Bohlin et al., 1983), consistent with the sightline towards recent star-forming sites.

The observed count rate on-target was $\sim 25,000$ counts sec^{-1} for a total exposure time (t_{exp}) of 250 seconds, resulting in a signal-to-noise ratio (S/N) per spectral resolution element of ~ 5 from $\lambda = 1020 - 1060$ Å and $S/N \gtrsim 10$ for $\lambda > 1100$ Å. The CHESS-2 echellogram of ϵ Per is shown in Figure 10.

5.1 Analysis of CHESS-2 data

The low S/N of the final flight data and diminished resolving power due to the fabrication error in the cross disperser meant that many of the primary science goals of CHESS were not achieved. We were unable to resolve any carbon-complex lines or achieve the signal needed to distinguish CO band absorption. However, the CHESS-2 spectrum of ϵ Per does show many absorption features between 1030 - 1220 Å, which we fit and analyzed to compare to previous observations of this sightline taken with Copernicus and IUE.

Scattered light from geo-coronal contamination posed a non-trivial amount of noise in the raw echellogram of CHESS-2. A combination of simulations

and laboratory measurements were used to estimate the scattered light background in the raw data. Scattered light simulations were performed using the ray-tracing software Zemax using the average flux of geo-coronal HI-Ly α at night (63×10^{-15} erg cm $^{-2}$ s $^{-1}$ arcsec $^{-2}$), and scattered light images were taken using an uncollimated Bayard-Albert tube fed with hydrogen-argon gas (France, 2006). Both produced consistent scattered light profiles, which were used to model the background noise of the flight echellogram. We note that even after extracting the modeled scattered light profile, it appears that an underlying scattered light residual still remained, which appears as excess flux in absorption features through the 1D spectrum. For example, several known saturated absorption features are not entirely bottomed-out to the zero-point of flux scale. *HST*-STIS suffers the same data reduction challenges due to the large scattered light profile of their mechanically-ruled gratings (Landsman & Bowers, 1997). Initial data reduction packages for STIS produced similar results - for example, either the over- or under-subtraction of background light (e.g., McGrath et al. 1999). STIS handles the complicated echelle-dominated background light profile with a 2-D algorithm that still has issues completely getting rid of the scattered light noise (Valenti et al. 2003 and references therein). This excess background noise in the CHESS observations is difficult to completely get rid of due to the low S/N of the observation, so we add this extra noise source into the errors in our analysis.

5.1.1 Metal Absorption Lines

We visually inspect the CHESS-2 spectrum of ϵ Per against the *IUE* and Copernicus spectra of the sightline. From this inspection, we select a number of stellar and interstellar absorption features that match well between all data sets. Next, we normalize the continuum of all data sets around the absorption lines of interest by fitting an arbitrary quadratic function through continuum points surrounding the absorption feature. Each absorption feature is fit with a Gaussian line profile using a reduced- χ^2 statistic. The initial conditions of the Gaussian fit are found to not drastically change the final result, so all line profiles begin with the same width parameter (σ). We then find the equivalent width (W_λ) of the each absorption line by finding the area under each Gaussian profile. This entire process is repeated for the same absorption lines found in *IUE* and Copernicus spectra.

Overall, we find good agreement between all three data sets. Figure 12 presents the normalized absorption lines for a large selection of metal feature from all three data sets, and Table 3 describes the quantities derived from each line profile, including the full width half maximum (FWHM) of each absorption line fit and W_λ derived from the line fits. Table 4 presents column density estimates from CHESS-2 and our re-analysis of *IUE* and Copernicus spectra of ϵ Per, along with the total column density of each species determined by Martin & York (1982) when available. We estimate a total column density of the species in the sightline ($N(X)$) by assuming the lines fit along the linear part of the curve of growth. We find good agreement in our estimates of $N(X)$

Table 3 ϵ Persei Metal Absorption Line Diagnostics & Comparison with Archival *IUE* and Copernicus Spectra

Ion	λ (\AA)	f	CHESS-2			<i>IUE</i>			Copernicus		
			FWHM (km/s)	W_λ (m \AA)	χ^2	FWHM (km/s)	W_λ (m \AA)	χ^2	FWHM (km/s)	W_λ (m \AA)	χ^2
H I	1025.72	0.079	1011	3646.6	156.60				743	3373.2	17.00
H I	1215.67	0.416	1835	7701.1	247.06	1620	6194.6	54.26			
C II	1334.53	0.129	131	190.8	1.21	99	347.6	0.51	124	360.0	1.13
C II	1335.71	0.115	69	208.6	1.25	63	448.6	0.99	93	316.9	1.35
C III	1175.26	0.272	440	624.1	31.73	561	2569.3	13.12	521	2763.5	11.8
N I	1134.98	0.040	75	35.1	3.04				60	95.5	1.15
N I	1199.26	0.133	37	36.3	3.27	40	150.5	7.67	53	84.7	6.23
N II	1083.99	0.101	65	74.0	2.03				157	121.9	1.16
N V	1238.82	0.156	113	209.3	12.12	283	339.6	10.28	325	407.9	5.27
N V	1242.80	0.078	270	330.6	12.32	220	509.6	13.37	307	322.7	7.28
O I	1302.17	0.052	218	302.8	15.59	160	430.1	10.41	242	467.2	50.29
S II	1259.52	0.016	64	69.0	2.22	28	42.6	2.23	52	66.6	1.07
Si II	1194.50	1.62	96	122.9	3.11	113	348.5	14.34	303	267.6	5.34
Si II	1197.39	0.323	69	107.9	12.13	92	161.8	17.18	101	260.7	8.03
Si III	1206.51	1.67	273	1151.2	2.94	473	1558.8	10.62	470	1337.1	5.78
Si IV	1393.76	0.528	570	1999.4	9.48	648	2698.0	16.71	637	2673.1	9.78
Si IV	1402.77	0.262	583	2077.3	5.68	481	2387.4	12.94	385	1906.1	5.15
P II	1152.81	0.236	51	22.1	0.89						
P II	1301.87	0.017	37	38.4	2.06	45	37.5	0.04	50	68.2	0.48

Table 4 ϵ Persei Metal Column Densities

Ion	$\log_{10}N(X)$			$\log_{10}N(X)$ (total)
	CHESS	<i>IUE</i>	Copernicus	Martin & York (1982)
C II	$16.3^{+0.3}_{-0.1}$	$16.6^{+0.1}_{-0.1}$	$16.6^{+0.2}_{-0.1}$	16.9
N I	$16.3^{+0.0}_{-0.6}$	$16.3^{+0.0}_{-0.1}$	$16.4^{+0.3}_{-0.3}$	16.3
N II	$16.3^{+0.1}_{-0.2}$		$16.5^{+0.2}_{-0.3}$	16.0
O I	$17.0^{+0.2}_{-0.1}$	$17.1^{+0.1}_{-0.1}$	$17.0^{+0.1}_{-0.2}$	17.2
S II	$16.9^{+0.2}_{-0.5}$	$16.6^{+0.1}_{-0.4}$	$16.8^{+0.4}_{-0.4}$	16.3
Si II	$15.4^{+0.4}_{-0.3}$	$15.6^{+0.3}_{-0.0}$	$15.8^{+0.4}_{-0.3}$	
P II	$13.6^{+0.2}_{-0.1}$	$13.5^{+0.1}_{-0.1}$	$13.8^{+0.0}_{-0.3}$	13.8

* Jenkins & Shaya (1979).

and Martin & York (1982) for all lines that overlap. For saturated lines (e.g., H I), we use the intrinsic properties of the line to estimate the column density in the sightline, which is the same approach used for our H₂ analysis below (see Section 5.1.2 for more details). We discuss the H I column density estimate from the CHESS-2 data in the following subsection.

5.1.2 H₂ Absorption Profile Fitting, Rotation Diagrams, and Formation Rates

Molecular hydrogen (H₂) is the most abundant constituent of interstellar clouds. Interstellar H₂ is observed as absorption features throughout the far-

UV regime along sightlines toward hot stars. Many H_2 interstellar sightlines display multiple temperature components (Spitzer et al., 1973), where the low rotation (J) lines ($J = 0, 1$) provide a measure of the kinetic (collision-dominated) gas temperature, while H_2 probed in higher rotational levels ($J > 3$) are sensitive to other physical processes, like UV-pumping (e.g., van Dishoeck & Black 1986), formation on dust grains (e.g., Jura 1974; Lacour et al. 2005) and heating by turbulence and/or shocks (e.g. Gry et al. 2002; Ingalls et al. 2011). The multi-component population structure provides important diagnostics about which processes dominate the physical cloud conditions and individual interstellar cloud properties, such as the total hydrogen density and the H_2 formation rate.

To analyze the properties of interstellar H_2 in the ϵ Per sightline, we determine the H_2 rotational structure following the procedure of France et al. 2013. We fit a multi-component H_2 absorption model to observed absorption features by combining the $\text{H}_2\text{OO1S}$ optical depth templates (McCandliss, 2003) and the MPFIT least-squares minimization routine (Markwardt, 2009). This method takes the theoretical line shape of each H_2 energy level for a given set of column density ($N(\text{H}_2)$) and Doppler- b values, convolves the synthetic spectrum with the line spread function (LSF) of the instrument, and adjusts $N(\text{H}_2)$ and b until a best-fit spectrum is found.

The ϵ Per spectrum is normalized to our model spectra around select H_2 absorption bands. We fit synthetic profiles simultaneously to the $\text{H}_2(1 - 0)$ (λ_0 1092.2 Å) and $\text{H}_2(0 - 0)$ (λ_0 1108.1 Å) complexes for low-to-intermediate rotational levels ($J'' = 0 - 7$). These bands are uncontaminated by other stellar and interstellar absorption features and have the highest S/N H_2 absorption features in our data set. To check the solutions of the $\text{H}_2(1 - 0)$ and $\text{H}_2(0 - 0)$ profile fits, we fit the modeled H_2 column densities to the $\text{H}_2(4 - 0)$ H_2 band (λ_0 1049.4 Å), which is also free of stellar and interstellar contaminants.

While it has been shown that the ϵ Per sightline may have upwards of four interstellar cloud components (Martin & York, 1982), the moderate spectral resolution of CHESS does not allow us to separate these different components. Therefore, assuming a single H_2 cloud, we find a b -value of 3.6 km s^{-1} , determined from the $\text{H}_2(J'' = 2 - 6)$ rotational levels, which are sensitive to changes in b . This value is consistent with previous curve-of-growth measurements of H_2 in the ϵ Per sightline (e.g., Stecher & Williams 1967; Carruthers 1971) and typical b -values for H_2 in the local ISM (Lehner et al., 2003; France et al., 2013).

We present the total H_2 column density and densities in each J -level in Table 5. The normalized spectra and best-fit models for the $\text{H}_2(4 - 0)$ and $\text{H}_2(1 - 0)+\text{H}_2(0 - 0)$ bands of ϵ Per are shown in Figure 13. We determine the total column density of H 1 ($N(\text{H } 1)_{obs}$) to be $\log_{10} N(\text{H } 1)_{obs} = 20.33 \pm 0.19$ from the Ly α absorption feature (λ 1215.67 Å) using the same procedure as the H_2 absorption fits (listed in Table 5). However, as noted in Diplas & Savage (1994), for B-stars, there is a non-negligible stellar contribution to the H 1-Ly α absorption profile, such that $N(\text{H } 1)_{obs} = N(\text{H } 1)_{stellar} + N(\text{H } 1)_{interstellar}$. For ϵ Per, Diplas & Savage (1994) found the total stellar H 1 column density

Table 5 ϵ Persei H_2 Parameters from CHESS-2 Observations and Model Fits

H_2 Level	$\log_{10}N(H_2, v''=0, J'')$ MPFIT Model	$\log_{10}N(H_2, v''=0, J'')$ MCMC Model
$J'' = 0$	$19.20^{+0.31}_{-0.02}$	19.65
$J'' = 1$	$19.56^{+0.42}_{-0.25}$	19.52
$J'' = 2$	17.35 ± 0.41	17.47
$J'' = 3$	$15.47^{+0.40}_{-0.32}$	15.66
$J'' = 4$	$14.75^{+0.68}_{-0.38}$	14.62
$J'' = 5$	$14.91^{+0.51}_{-0.48}$	14.61
$J'' = 6$	$13.12^{+0.50}_{-0.42}$	13.51
$J'' = 7$	< 13.51	13.40
$\log_{10}N(H_2)$	19.72 ± 0.35	19.83 ± 0.02
$\log_{10}N(H\ 1)$	20.31 ± 0.19	20.43 ± 0.07
T_{01}	95 ± 2 K	95 ± 1 K
T_{exc}	500 ± 150 K	
b_{H_2}	3.6 ± 0.6 km s $^{-1}$	3.6 km s $^{-1}$
$f(H_2)$	0.24 ± 0.05	0.30 ± 0.03
Rn		49.5×10^{-16} s $^{-1}$
n_H		55 cm $^{-3}$

to be $\log_{10}N(H\ 1)_{stellar} = 18.82$, so the total *interstellar* column density of neutral hydrogen is $\log_{10}N(H\ 1) = 20.31 \pm 0.19$. We use $N(H\ 1)$ and $N(H_2)$ to calculate the molecular fraction ($f(H_2)$) of the interstellar cloud:

$$f(H_2) = \frac{2N(H_2)}{N(HI) + 2N(H_2)} = 0.24 \pm 0.05. \quad (1)$$

The homonuclear nature of the hydrogen molecule forbids radiative transitions from $J'' = 1 \rightarrow 0$ within the same electronic band, while quadrupole transitions from $J'' = 2 \rightarrow 0$ are allowed but slow ($A_{2 \rightarrow 0} \approx 3 \times 10^{-11}$ s $^{-1}$; Wolniewicz et al. 1998). Therefore, for a sightline with an appreciable density of hydrogen through the ISM, collisions are expected to control the level populations of the lower energy J'' states (0, 1, 2). We can therefore define a kinetic temperature, T_{01} , which describes the collision-dominated regime of the interstellar cloud. T_{01} is derived from the ratio of column densities in the $J'' = 0$ and $J'' = 1$ levels:

$$N(J'' = 1)/N(J'' = 0) = \frac{g_1}{g_0} e^{(-E_{01}/kT_{01})} = 9e^{(-171K/T_{01})} \quad (2)$$

where g_1 and g_0 are the statistical weights in the $J'' = 1$ and 0 levels, respectively. We find that the kinetic temperature of the H_2 in the ϵ Per sightline is $T_{01} = 95 \pm 2$ K.

The temperature of the higher rotational levels ($J'' > 3$) can be fit with an ‘‘excitation’’ temperature, T_{exc} , by determining the slope of the rotation diagram between $J'' = 3 - 7$. A least-squares linear fit through these rotation levels found $T_{exc} = 500 \pm 150$ K (Figure 14, left).

We use the new results from the CHESS-2 observations to measure these two interstellar physical cloud parameters in the ϵ Per sightline. First, we derive Rn and n_H from two empirical approaches: the first from Martin & York

Table 6 Physical Cloud Conditions of ϵ Persei, Derived from Analytic Solutions

Method:	Martin & York (1982)	Gry et al. (2002)
Rn (s^{-1})	45.6×10^{-16}	6.6×10^{-16}
n_H^a (cm^{-3})	150	20
n_H^b (cm^{-3})	80	10
n_H^c (cm^{-3})	10	1.5

^a $R = 3.0 \times 10^{-17} \text{ cm}^3 \text{ s}^{-1}$; Jura (1975b).

^b $R = 6.0 \times 10^{-18} \text{ T}^{1/2} \text{ cm}^3 \text{ s}^{-1}$, assuming $T = T_{01} = 95 \text{ K}$; Black & van Dishoeck (1987).

^c $R = 7.3 \times 10^{-17} (\text{T} / 100)^{1/2} \langle \epsilon_{gr} \rangle \Sigma_{-21} \text{ cm}^3 \text{ s}^{-1}$, assuming $T = T_{01} = 95 \text{ K}$, $\Sigma_{-21} =$ the grain surface area for silicate-graphite PAHs $= 6.0 (\times 10^{-21}) \text{ cm}^2 \text{ H}^{-1}$, and $\langle \epsilon_{gr} \rangle =$ the average efficiency for H_2 formation on dust grains ~ 1.0 , which gives a lower limit to n_H ; Weingartner & Draine (2001); Draine (2011).

(1982), who use an updated prescription to a common approach (e.g., Jura 1975b) to define diffuse ISM physical cloud conditions, and the second from Gry et al. (2002), who take into account additional physical mechanisms important for denser clouds, like dust and molecular shielding and irradiation. The Martin & York (1982) analysis calculates Rn based on the formalism presented in Jura (1975b): $Rn \approx N(\text{H}_2; J=4) / N(\text{H } 1)(4.28 \times 10^8)$. Using the column densities derived from the CHESS-2 observation, we find $Rn = 45.6 \times 10^{-16} \text{ s}^{-1}$. The Gry et al. (2002) method balances formation and destruction rates of H_2 : $Rn = 0.5 \frac{f}{1-f} \beta_0 \langle S \rangle$, where f is the molecular fraction of H_2 in the interstellar cloud, β_0 is the mean rate of H_2 photo-dissociation in the diffuse local interstellar medium, and $\langle S \rangle$ is the mean self-shielding factor of H_2 against photo-dissociation from the UV radiation source. For the diffuse ISM, β_0 is defined as $5.0 \times 10^{-11} \text{ s}^{-1}$ (e.g., Habing 1968; Mathis et al. 1983). We find $\langle S \rangle \approx 8.2 \times 10^{-5}$ using Equation 37 in Draine & Bertoldi (1996), which depends on $N(\text{H}_2)$ and b derived from our synthetic absorption spectra (Section 5.1.2). We find $Rn \approx 7.5 \times 10^{-16} \text{ s}^{-1}$ using the Gry et al. (2002) approach, which is ~ 6 times lower than Rn derived using the Martin & York (1982) method. Table 6 presents the H_2 formation rates and resulting realizations of n_H using R found from Jura (1975b), Black & van Dishoeck (1987), and Draine (2011).

There are roughly two dex in spread for n_H between these two methods, depending on the adopted H_2 formation rate. To better constrain Rn and n_H in the ϵ Per sightline, we create stationary H_2 equilibrium models, which populate H_2 energy levels based on the physical conditions of an interstellar cloud. We follow the framework presented by Draine & Bertoldi (1996) (Equations 1 - 14), Gry et al. (2002), and references therein. The models balance excitation and de-excitation processes working on H_2 , including formation pumping, H_2 dissociation, photo-excitation, spontaneous decay, and collisional de-excitation.

The UV radiation field is assumed to be dominated by the blackbody UV continuum produced by ϵ Per. Interstellar H_2 is excited to higher energy electronic levels by this UV radiation, where it either fluoresces back to the ground electronic energy state or dissociates. Energy levels, transition probabilities, and dissociation probabilities for fluorescent transitions are adapted from Ab-

grall & Roueff (1989), Abgrall et al. (1992, 1993a), and Abgrall et al. (1993b). Spontaneous decay rates of ground-level quadrupole transitions are taken from Wolniewicz et al. (1998). Finally, collisional de-excitation of H_2 is calculated from equations and coefficients presented by Mandy & Martin (1993) and Martin & Mandy (1995), where hydrogen is the dominate collisional partner of H_2 .

We allow Rn and n_H to float but constrain the values of n_H between the minimum and maximum values presented in Table 6. We assume that $n(\text{H})$, $n(\text{H}_2)$, and n_H are uniformly distributed across the interstellar cloud slab, which allows us to retrieve $N(\text{H}_2)$ and $N(\text{H I})$ from our simulations, and Rn does not vary across the modeled region. The models are run through a Markov Chain Monte Carlo (MCMC) routine, performed with the Python `emcee` package (Foreman-Mackey et al., 2013) in the same manner as described in Hoadley et al. (2017). The routine is run with 100 walkers over 500 individual steps. The MCMC analysis produces comparable molecular and atomic hydrogen column densities compared to our direct observational results: $\log_{10}N(\text{H}_2) = 19.83 \pm 0.02$ and $\log_{10}N(\text{H I}) = 20.43 \pm 0.07$, with the same kinetic temperature: $T_{01}(\text{H}_2) = 95 \pm 1$ K. The formation rate and hydrogen density in the physical cloud model are found to be $Rn = 49.5 \times 10^{-16} \text{ s}^{-1}$ and $n_H = 55 \text{ cm}^{-3}$. Our results are slightly larger values than diffuse cloud conditions of ϵ Per determined by Jura (1975a) and Martin & York (1982) and much larger than the denser interstellar cloud schematic of Gry et al. (2002), making our results consistent with a diffuse interstellar cloud origin (Jura, 1975b). Our results find that the volumetric formation rate of H_2 in the ϵ Per sightline is $R = 9.0 \times 10^{-17} \text{ cm}^3 \text{ s}^{-1}$. Assuming the gas density is uniform, we find that the interstellar cloud probed in the sightline extends ~ 0.4 pc.

We show the best-fit H_2 equilibrium models, along with the CHES-2 H_2 rotation diagram for ϵ Per, in Figure 14 (right). Our resulting H_2 formation rate is slightly higher than the classic formation rates presented by Jura (1975b) and Black & van Dishoeck (1987) (Table 6). This can be accounted for in a few ways: either the efficiency of H_2 formation on silicate-dominated dust grains is higher than expected ($\langle \epsilon_{gr} \rangle \sim 20\%$), or the distribution of dust grain sizes in the ϵ Per sightline deviates from the canonical distribution assumed for the average Milky Way ISM (Weingartner & Draine, 2001).

6 Conclusions

The Colorado High-resolution Echelle Stellar Spectrograph (CHES-2) is a UV spectroscopic instrument meant to demonstrate high-throughput, high-resolution far-UV spectroscopy. Such concepts are especially important for pathfinders of upcoming space missions, where future observatories will have to address key observational capabilities when *HST* is no longer available. In addition, CHES-2 provides an ideal platform to improve and test experimental technologies meant to vastly improve the performance of diffraction gratings, mirror coatings, and detector efficiencies throughout the UV.

For the first two launches of CHES, we tested and flew different high-order diffraction gratings (echelles) for UV spectroscopy and demonstrated the improved performance and dynamic range of state-of-the-art MCP detectors. In the end, both the underwhelming performance of the experimental echelle gratings and an error in the ruling of the toroidal surface figure cross-dispersing grating proved detrimental to the overall performance of the spectrograph. Still, the first two launches of the instrument gathered data on the stellar sightlines they observed, with the second flight acquiring adequate S/N to perform a detailed analysis of the interstellar sightline. We find many different metallic absorption lines in the ϵ Per sightline, and we fit multiple H_2 band complexes with thermal and stationary equilibrium models to characterize the H_2 in this diffuse ISM sightline. We find the column density and temperature of cool H_2 to be consistent with analyses performed with Copernicus and find that the full stationary equilibrium model suitably fits the observed column densities of all J states.

The CHES experiment went on to observe nearby early B-type stars to study the molecular properties of local interstellar clouds aboard two additional NASA-funded sounding rocket missions: the third launch of CHES took place at WSMR in June 2017 and successfully observed the sightline towards β Sco¹ (Kruczek et al., 2017), while the fourth and final launch took off from the Kwajalein Test Range in April 2018 and observed γ Arae (Kruczek et al., 2018). A detailed analysis of both sightlines, paired with an analysis of archival spectral datasets obtained with Copernicus and *FUSE*, has shown that previous studies overestimate the average gas kinetic temperature of the diffuse molecular ISM by 12% (Kruczek et al., 2019).

We acknowledge the hard work and dedication of the NASA WFF/NSROC payload team, the Physical Sciences Laboratory at New Mexico State University, and the Navy team at WSMR that supported the NASA/CU 36.297 UG. We thank the referee of this manuscript for their helpful suggestions and points where further clarification was warranted. KH would like to acknowledge the generous support and guidance from Prof. Jim Green, Ted Schultz, Michael Kaiser, and the University of Colorado UV sounding rocket research group during the build and operations of CHES-I and CHES-II. KH would also like to thank Dr. Nicholas Kruczek, Jacob Wilson, Jack Swanson, and Nicholas Erickson for each of their individual contributions and achievements that led to a successful CHES-II flight, subsequent CHES successes, and their invaluable moral support before, during, and after the mission. KH acknowledges support by the David & Ellen Lee Postdoctoral Fellowship in Experiment Physics at Caltech. This research was funded by the NASA Astrophysics Research and Analysis (APRA) grant NNX13AF55G. AY acknowledges support by an appointment to the NASA Postdoctoral Program at Goddard Space Flight Center, administered by the Universities Space Research Association through a contract with NASA.

References

- Abgrall, H., Le Bourlot, J., Pineau Des Forets, G., Roueff, E., Flower, D. R., & Heck, L. 1992, *A&A*, 253, 525
- Abgrall, H. & Roueff, E. 1989, *A&AS*, 79, 313
- Abgrall, H., Roueff, E., Launay, F., Roncin, J. Y., & Subtil, J. L. 1993a, *A&A*, 101, 273
- . 1993b, *A&A*, 101, 323
- Beasley, M., Burgh, E., & France, K. 2010, in *Proc. SPIE, Vol. 7732, Space Telescopes and Instrumentation 2010: Ultraviolet to Gamma Ray*, 773206
- Black, J. H. & van Dishoeck, E. F. 1987, *ApJ*, 322, 412
- Blasberger, A., Behar, E., Perets, H. B., Brosch, N., & Tielens, A. G. G. M. 2017, *ApJ*, 836, 173
- Bohlin, R. C., Jenkins, E. B., Spitzer, Jr., L., York, D. G., Hill, J. K., Savage, B. D., & Snow, Jr., T. P. 1983, *ApJS*, 51, 277
- Burgh, E. B., France, K., & Jenkins, E. B. 2010, *ApJ*, 708, 334
- Burgh, E. B., France, K., & McCandliss, S. R. 2007, *ApJ*, 658, 446
- Carruthers, G. R. 1971, *ApJ*, 166, 349
- Diplas, A. & Savage, B. D. 1994, *ApJ*, 93, 211
- Draine, B. T. 2011, *Physics of the Interstellar and Intergalactic Medium*
- Draine, B. T. & Bertoldi, F. 1996, *ApJ*, 468, 269
- Federman, S. R., Glassgold, A. E., Jenkins, E. B., & Shaya, E. J. 1980, *ApJ*, 242, 545
- Foreman-Mackey, D., Hogg, D. W., Lang, D., & Goodman, J. 2013, *PASP*, 125, 306
- France, K., Beasley, M., Kane, R., Nell, N., Burgh, E. B., & Green, J. C. 2012, in *Proc. SPIE, Vol. 8443, Space Telescopes and Instrumentation 2012: Ultraviolet to Gamma Ray*, 844305
- France, K., Fleming, B., & Hoadley, K. 2016a, *Journal of Astronomical Telescopes, Instruments, and Systems*, 2, 041203
- France, K., Hoadley, K., Fleming, B. T., Kane, R., Nell, N., Beasley, M., & Green, J. C. 2016b, *Journal of Astronomical Instrumentation*, 5, 1640001
- France, K., Nell, N., Kane, R., Burgh, E. B., Beasley, M., & Green, J. C. 2013, *ApJL*, 772, L9
- France, K. C. 2006, PhD thesis, The Johns Hopkins University
- Green, J. C., Froning, C. S., Osterman, S., Ebbets, D., Heap, S. H., Leitherer, C., Linsky, J. L., Savage, B. D., Sembach, K., Shull, J. M., Siegmund, O. H. W., Snow, T. P., Spencer, J., Stern, S. A., Stocke, J., Welsh, B., Béland, S., Burgh, E. B., Danforth, C., France, K., Keeney, B., McPhate, J., Penton, S. V., Andrews, J., Brownsberger, K., Morse, J., & Wilkinson, E. 2012, *ApJ*, 744, 60
- Gry, C., Boulanger, F., Nehmé, C., Pineau des Forêts, G., Habart, E., & Falgarone, E. 2002, *A&A*, 391, 675
- Habing, H. J. 1968, *BAIN*, 19, 421
- Hamden, E. T., Schiminovich, D., & Seibert, M. 2013, *ApJ*, 779, 180

- Hoadley, K., France, K., Arulanantham, N., Parke Loyd, R. O., & Kruczek, N. 2017, ArXiv e-prints
- Hoadley, K., France, K., Kruczek, N., Fleming, B., Nell, N., Kane, R., Swanson, J., Green, J., Erickson, N., & Wilson, J. 2016, in Proc. SPIE, Vol. 9905, Society of Photo-Optical Instrumentation Engineers (SPIE) Conference Series, 99052V
- Hoadley, K., France, K., Nell, N., Kane, R., Schultz, T., Beasley, M., Green, J., Kulow, J., Kersgaard, E., & Fleming, B. 2014, in Proc. SPIE, Vol. 9144, Space Telescopes and Instrumentation 2014: Ultraviolet to Gamma Ray, 914406
- Hoadley, K., Martin, D. C., Metzger, B. M., Seibert, M., McWilliam, A., Shen, K. J., Neill, J. D., Stefansson, G., Monson, A., & Schaefer, B. E. 2020, *Nature*, Accepted for Publication
- Hoffleit, D. & Jaschek, C. 1982, *The Bright Star Catalogue*. Fourth revised edition.
- Indebetouw, R., McLean, R., Wilkinson, E., Green, J., & Beasley, M. 2001, *Review of Scientific Instruments*, 72, 1850
- Ingalls, J. G., Bania, T. M., Boulanger, F., Draine, B. T., Falgarone, E., & Hily-Blant, P. 2011, *ApJ*, 743, 174
- Jenkins, E. B., Joseph, C. L., Long, D., Zucchino, P. M., & Carruthers, G. R. 1988, in Proc. SPIE, Vol. 932, *Ultraviolet technology II*, ed. R. E. Huffman, 213–229
- Jenkins, E. B., Reale, M. A., Zucchino, P. M., & Sofia, U. J. 1996, *A&SS*, 239, 315
- Jenkins, E. B. & Shaya, E. J. 1979, *ApJ*, 231, 55
- Jenkins, E. B. & Tripp, T. M. 2001, *ApJS*, 137, 297
- Jura, M. 1974, *ApJ*, 191, 375
- . 1975a, *ApJ*, 197, 581
- . 1975b, *ApJ*, 197, 575
- Kane, R., Beasley, M., Green, J., Burgh, E., & France, K. 2011, in Proc. SPIE, Vol. 8145, Society of Photo-Optical Instrumentation Engineers (SPIE) Conference Series, 81450P
- Kimble, R. A., Woodgate, B. E., Bowers, C. W., Kraemer, S. B., Kaiser, M. E., Gull, T. R., Heap, S. R., Danks, A. C., Boggess, A., Green, R. F., Hutchings, J. B., Jenkins, E. B., Joseph, C. L., Linsky, J. L., Maran, S. P., Moos, H. W., Roesler, F., Timothy, J. G., Weistrop, D. E., Grady, J. F., Loiacono, J. J., Brown, L. W., Brumfield, M. D., Content, D. A., Feinberg, L. D., Isaacs, M. N., Krebs, C. A., Krueger, V. L., Melcher, R. W., Rebar, F. J., Vitagliano, H. D., Yagelowich, J. J., Meyer, W. W., Hood, D. F., Argabright, V. S., Becker, S. I., Bottema, M., Breyer, R. R., Bybee, R. L., Christon, P. R., Delamere, A. W., Dorn, D. A., Downey, S., Driggers, P. A., Ebbets, D. C., Gallegos, J. S., Garner, H., Hetlinger, J. C., Lettieri, R. L., Ludtke, C. W., Michika, D., Nyquist, R., Rose, D. M., Stocker, R. B., Sullivan, J. F., Van Houten, C. N., Woodruff, R. A., Baum, S. A., Hartig, G. F., Balzano, V., Biagetti, C., Blades, J. C., Bohlin, R. C., Clampin, M., Doxsey, R., Ferguson, H. C., Goudfrooij, P., Hulbert, S. J., Kutina, R., McGrath, M.,

- Lindler, D. J., Beck, T. L., Feggans, J. K., Plait, P. C., Sandoval, J. L., Hill, R. S., Collins, N. R., Cornett, R. H., Fowler, W. B., Hill, R. J., Landsman, W. B., Malumuth, E. M., Standley, C., Blouke, M., Gruszczak, A., Reed, R., Robinson, R. D., Valenti, J. A., & Wolfe, T. 1998, *ApJL*, 492, L83
- Kruczek, N., France, K., Hoadley, K., Fleming, B., & Nell, N. 2019, *ApJ*, 878, 77
- Kruczek, N., France, K., Hoadley, K., Fleming, B., Nell, N., Kane, R., & Beatty, D. 2017, in *Space Telescopes and Instrumentation 2017*, Proc. SPIE
- Kruczek, N., Nell, N., France, K., Hoadley, K., Fleming, B., Ulrich, S., Miller, A. D., Egan, A., Witt, E., & Kane, R. 2018, in *Society of Photo-Optical Instrumentation Engineers (SPIE) Conference Series*, Vol. 10699, Society of Photo-Optical Instrumentation Engineers (SPIE) Conference Series, 106990K
- Lacour, S., Ziskin, V., Hébrard, G., Oliveira, C., André, M. K., Ferlet, R., & Vidal-Madjar, A. 2005, *ApJ*, 627, 251
- Landsman, W. & Bowers, C. 1997, in *The 1997 HST Calibration Workshop with a New Generation of Instruments*, ed. S. Casertano, R. Jedrzejewski, T. Keyes, & M. Stevens, 132
- Lehner, N., Jenkins, E. B., Gry, C., Moos, H. W., Chayer, P., & Lacour, S. 2003, *ApJ*, 595, 858
- Ma, X.-Y., Zhu, Y.-Y., Yan, Q.-B., You, J.-Y., & Su, G. 2020, *MNRAS*
- Mandy, M. E. & Martin, P. G. 1993, *ApJ*, 86, 199
- Markwardt, C. B. 2009, in *Astronomical Society of the Pacific Conference Series*, Vol. 411, *Astronomical Data Analysis Software and Systems XVIII*, ed. D. A. Bohlender, D. Durand, & P. Dowler, 251
- Martin, D. C., Fanson, J., Schiminovich, D., Morrissey, P., Friedman, P. G., Barlow, T. A., Conrow, T., Grange, R., Jelinsky, P. N., Milliard, B., Siegmund, O. H. W., Bianchi, L., Byun, Y.-I., Donas, J., Forster, K., Heckman, T. M., Lee, Y.-W., Madore, B. F., Malina, R. F., Neff, S. G., Rich, R. M., Small, T., Surber, F., Szalay, A. S., Welsh, B., & Wyder, T. K. 2005, *ApJL*, 619, L1
- Martin, D. C., Seibert, M., Neill, J. D., Schiminovich, D., Forster, K., Rich, R. M., Welsh, B. Y., Madore, B. F., Wheatley, J. M., Morrissey, P., & Barlow, T. A. 2007, *Nature*, 448, 780
- Martin, E. R. & York, D. G. 1982, *ApJ*, 257, 135
- Martin, P. G. & Mandy, M. E. 1995, *ApJL*, 455, L89
- Mathis, J. S., Mezger, P. G., & Panagia, N. 1983, *A&A*, 128, 212
- McCandliss, S. R. 2003, *PASP*, 115, 651
- McCord, M. A. & Rooks, M. J. 2000, *SPIE Handbook of Microlithography, Micromachining and Microfabrication*, Vol. 1 (SPIE)
- McGrath, M. A., Busko, I., & Hodge, P. 1999, *Calstis6: Extraction of 1-D Spectra in the STIS Calibration Pipeline*, Tech. rep.
- Morton, D. C. 1975, *ApJ*, 197, 85
- Redfield, S. 2006, in *Astronomical Society of the Pacific Conference Series*, Vol. 352, *New Horizons in Astronomy: Frank N. Bash Symposium*, ed. S. J. Kannappan, S. Redfield, J. E. Kessler-Silacci, M. Landriau, & N. Drory, 79

- Sahai, R. & Chronopoulos, C. K. 2010, *ApJL*, 711, L53
- Sasian, J. 1997, *Optical Engineering*, 36, 183
- Savage, B. D., Bohlin, R. C., Drake, J. F., & Budich, W. 1977, *ApJ*, 216, 291
- Scowen, P. A., Tripp, T., Beasley, M., Ardila, D., Andersson, B.-G., Maíz Apellániz, J., Barstow, M., Bianchi, L., Calzetti, D., Clampin, M., Evans, C. J., France, K., García García, M., Gomez de Castro, A., Harris, W., Hartigan, P., Howk, J. C., Hutchings, J., Larruquert, J., Lillie, C. F., Matthews, G., McCandliss, S., Polidan, R., Perez, M. R., Rafelski, M., Roederer, I. U., Sana, H., Sanders, W. T., Schiminovich, D., Thronson, H., Tumlinson, J., Vallerga, J., & Wofford, A. 2017, *PASP*, 129, 076001
- Siegmund, O. H. W., Tremsin, A. S., & Vallerga, J. V. 2009, in *Proc. SPIE*, Vol. 7435, *UV, X-Ray, and Gamma-Ray Space Instrumentation for Astronomy XVI*, 74350L
- Snow, T. P. & McCall, B. J. 2006, *ARA&A*, 44, 367
- Spitzer, L., Drake, J. F., Jenkins, E. B., Morton, D. C., Rogerson, J. B., & York, D. G. 1973, *ApJL*, 181, L116
- Stecher, T. P. & Williams, D. A. 1967, *ApJL*, 149, L29
- The LUVVOIR Team. 2019, arXiv e-prints, arXiv:1912.06219
- Thomas, R. J. 2003, in *Proc. SPIE*, Vol. 4853, *Innovative Telescopes and Instrumentation for Solar Astrophysics*, ed. S. L. Keil & S. V. Avakyan, 411–418
- Tumlinson, J., Peeples, M. S., & Werk, J. K. 2017, *ARA&A*, 55, 389
- Valenti, J., Busko, I., Quijano, J. K., Lindler, D., & Bowers, C. W. 2003, in *HST Calibration Workshop : Hubble after the Installation of the ACS and the NICMOS Cooling System*, ed. S. Arribas, A. Koekemoer, & B. Whitmore, 209
- Vallerga, J., Raffanti, R., Tremsin, A., Siegmund, O., McPhate, J., & Varner, G. 2010, in *Proc. SPIE*, Vol. 7732, *Space Telescopes and Instrumentation 2010: Ultraviolet to Gamma Ray*, 773203
- van Dishoeck, E. F. & Black, J. H. 1986, *ApJS*, 62, 109
- Weingartner, J. C. & Draine, B. T. 2001, *ApJ*, 548, 296
- Wolniewicz, L., Simbotin, I., & Dalgarno, A. 1998, *ApJ*, 115, 293
- Woodruff, R. A., Danchi, W. C., Heap, S. R., Hull, T., Kendrick, S. E., Purves, L. R., Rhee, M. S., Mentzell, E., Fleming, B., Valente, M., Burge, J., Lewis, B., Dodson, K., Mehle, G., & Tomic, M. 2019, *Journal of Astronomical Telescopes, Instruments, and Systems*, 5, 024006

List of Figures

- 1 The Zemax ray trace of CHESS, including the secondary aspect camera system. The mechanical collimator reduces stray light in the line of sight and feeds starlight to the echelle. The echelle disperses UV light into high-dispersion orders, which are focused by the cross disperser onto the detector plane. The different colored lines represent a series of wavelengths across the 1000 – 1600 Å bandpass. Adapted from Hoadley et al. (2016). 28
- 2 Schematic view of the Colorado High-resolution Echelle Stellar Spectrograph (CHESS). Dimensions defined are in centimeters. The optical path (dashed purple line) follows right to left, with the target light entering the instrument when the shutter door is open during flight. Adapted from Hoadley et al. (2014) and Hoadley et al. (2016). 29
- 3 A comparison of echelle gratings tested for use in the CHESS instrument. We include the best-performing echelle gratings from the lithography etching R&D project undertaken by LightSmyth, Inc. (flown on CHESS-1, 36.285 UG), the e-beam samples fabricated by JPL, and two mechanically-ruled replica gratings from Bach Research, Inc. and Richardson Gratings, respectively. Both mechanically-ruled gratings out-performed the R&D echelles and met the CHESS minimum order efficiency threshold. Adapted from Hoadley et al. (2016). 30
- 4 The measured reflectivity (order efficiency \times reflectivity of Al+LiF) of the cross dispersing grating in CHESS over time, overplotted with simple spline curves to show the resemblance of each trial. The colored points and lines represent times before and after the CHESS-1 and CHESS-2 missions that the cross disperser grating efficiency was measured: pre-36.285 (blue) is before the cross disperser was installed and aligned into the instrument for the CHESS-1 flight, post-36.285 (red) is right after we recovered the instrument after the CHESS-1 flight and measured the post-flight efficiency of all the optical components, and pre-36.297 (green) is before the grating was installed and aligned into the instrument structure for the CHESS-2 flight. We focus on the reflectivity of the $m = -1$ order, which is the dispersion order used in the CHESS instrument. Because Al+LiF can exhibit efficiency degradations when not stored in a dry environment, we measure how the order reflectivity changes between CHESS-1 and CHESS-2 without re-coating the optic. No significant degradation of the coating has been measured between the first two flights of CHESS. Adapted from Hoadley et al. (2016). 31

5 *Left:* Performance (for each grating: peak order efficiency, and for the detector: detector quantum efficiency) of all optical components of CHESSE-2. For the first flight of CHESSE, the only component performance that changed significantly was the echelle efficiency, which was $\ll 0.1$ (10%) across the bandpass. *Right:* The CHESSE-2 effective area, including throughput loss from baffling, compared to the effective area of CHESSE-1. The total effective area of CHESSE-2 is about an order of magnitude larger than that of CHESSE-1, owing primarily to the large gain in echelle order efficiency across the bandpass. Adapted from Hoadley et al. (2016). 32

6 Presented are the raw images of the CHESSE-1 (left) and CHESSE-2 (right; edge effects have been cropped out) echellograms from pre-flight calibrations (March 2014 and December 2015) using an arc lamp flowing 65%/35% H/Ar gas. The brightest feature in both images is H I-Ly α (λ 1215.67 Å); the CHESSE-1 echellogram only shows Ly α in one echelle order, while the CHESSE-2 echellogram disperses Ly α photons into two adjacent echelle orders. The other broad feature(s) visible in the CHESSE-2 echellogram are HI-Ly β (1025.72 Å), about 1/4 of the way from the top of the image, and HI-Ly γ (97.25 Å), barely visible above the Ly β features. The more discrete features dotted throughout the spectrum are H₂ emission from electron-impact fluorescence. Adapted from Hoadley et al. (2014) and Hoadley et al. (2016). 33

7 The complete first-order wavelength solution for the pre-launch CHESSE-2 calibration spectra from $\lambda\lambda$ 900 - 1750 Å. The final wavelength solution was determined using H₂ fluorescence emission features and a functional extrapolation of the wavelength with a 6th-order polynomial fit. Over-plotted in magenta is the model H₂ fluorescence inside the arc lamp ($T_{eff} = 800$ K, $N(\text{H}_2) \sim 10^{19}$ cm⁻², $E_{electron} = 50$ eV). The spectrum is scaled to the highest total counts of the H₂ features; otherwise, Ly α would dominate the spectrum and the H₂ features would be washed out. To show how neighboring order spectra overlap and correlate to form the final 1D spectrum, individual order spectra have been plotted in different colors. Adapted from Hoadley et al. (2016). 34

8 The line spread function (LSF) fits of H₂ emission features in one order of the pre-launch calibration spectrum of CHESSE-2 (echelle order $m = 286$). The order spectrum is shown in black. Red and blue Gaussian line fits are shown for the narrow and broad Gaussian fits for each line, respectively. The green line is the sum of all Gaussian components to reproduce the spectrum. A modeled H₂ fluorescence spectrum is shown in magenta. Adapted from Hoadley et al. (2016). 35

- 9 The False-color representation of the flight echellogram from CHESS-1, taken on 24 May 2014, of α Vir. The purple/black regions represent areas with lower concentrations of photon counts, and blue/green pixels represent pixels with higher concentrations of photons collected. Marked with green arrows and labeled are the most prominent features in the echellogram. Because of the low S/N of the flight data, the echellogram has been binned to 512×512 , to show absorption features in the image. Adapted from Hoadley et al. (2014). 36
- 10 The raw, false-color echellogram of ϵ Per, recorded over $t_{exp} \sim 250$ sec on NASA/CU mission 36.297 UG (CHESS-2). Along the right, we mark the rough wavelength coverage as a function of the detector y axis. In an individual echelle order, wavelength increases to the right. Stellar continuum through the far-UV acts as a back-light behind the interstellar material. Dark streaks in the continuum show stellar and interstellar atoms, ions, and molecules absorbing photons at specific wavelengths; prominent interstellar and stellar features are labeled with arrows pointing to the absorption lines and the absorption species along the left. Adapted from Hoadley et al. (2016). 37
- 11 The flux-calibrated CHESS-2 spectra of ϵ Per from $\lambda = 1020 - 1550$ Å. Representative error bars are shown in red. The CHESS-2 spectrum was flux-calibrated against *IUE* spectra of ϵ Per, and the continuum shape was compared with *Copernicus* spectra at $\lambda < 1150$ Å. Prominent stellar and interstellar absorption features are shown using vertical lines: purple lines show H₂ absorption features from $v = 0, J = 0 - 7$, orange lines show H I absorption, green lines show carbon, oxygen, and nitrogen species, and blue lines mark heavier metals (iron, silicon, sulfur, argon, magnesium, nickel, and copper). 38
- 12 (a) We present the normalized absorption features of different phases of interstellar carbon observed in the CHESS (left panels), Copernicus (middle panels), and *IUE* (right panels) FUV spectra of ϵ Per. We fit all lines with a Gaussian profile (blue dashed line) and determine the equivalent width (W_λ) from the area under the Gaussian (green hashed area). We determine W_λ for many metal lines found throughout the FUV in all data sets over a variety of interstellar phases - a comprehensive list of results is presented in Table 3. 39
- 12 (b) Continued; different phases of nitrogen observed by CHESS, Copernicus, and *IUE*, their Gaussian fits (blue dashed line), and W_λ (green shaded area). 40
- 12 (c) Continued; different phases of silicon observed by CHESS, Copernicus, and *IUE*, their Gaussian fits (blue dashed line), and W_λ (green shaded area). 41

-
- 12 (d) Continued; phosphorus, hydrogen, and sulfur observed by CHESS, Copernicus, and *IUE*, their Gaussian fits (blue dashed line), and W_λ (green shaded area). 42
- 13 Synthetic H_2 profile fits for the $H_2(4 - 0)$ band (*left*) and $H_2(1 - 0)$ and $H_2(0 - 0)$ bands (*right*), shown in red, are overlaid on top of the ϵ Per spectrum. Molecular rotational levels are labeled with purple dashes. The best-fit Doppler velocities for all three spectral band fits is $b = 3.6 \text{ km s}^{-1}$ 43
- 14 We present the ϵ Per H_2 rotation diagram with two different model fits. *Left*: The H_2 rotation diagram is fit assuming the sightline has two temperature populations of H_2 : a cool, kinetic temperature, described by T_{01} (pink), and a warmer, “excitation” temperature, described by T_{exc} (blue). *Right*: The H_2 rotation diagram is fit with an H_2 equilibrium model (purple asterisks), which includes affects from UV-photon pumping, collisions with other particles, and formation/destruction rates of H_2 in a diffuse medium. The kinetic temperature derived from these models is shown in orange. 44

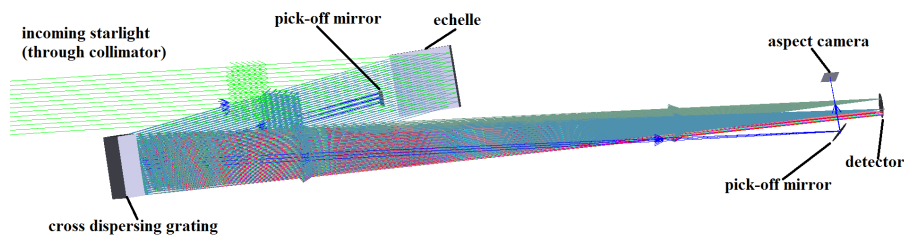


Fig. 1 The Zemax ray trace of CHESS, including the secondary aspect camera system. The mechanical collimator reduces stray light in the line of sight and feeds starlight to the echelle. The echelle disperses UV light into high-dispersion orders, which are focused by the cross disperser onto the detector plane. The different colored lines represent a series of wavelengths across the 1000 – 1600 Å bandpass. Adapted from Hoadley et al. (2016).

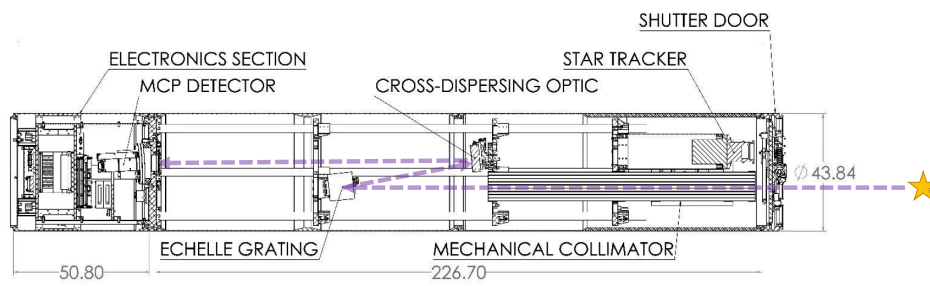


Fig. 2 Schematic view of the Colorado High-resolution Echelle Stellar Spectrograph (CHES). Dimensions defined are in centimeters. The optical path (dashed purple line) follows right to left, with the target light entering the instrument when the shutter door is open during flight. Adapted from Hoadley et al. (2014) and Hoadley et al. (2016).

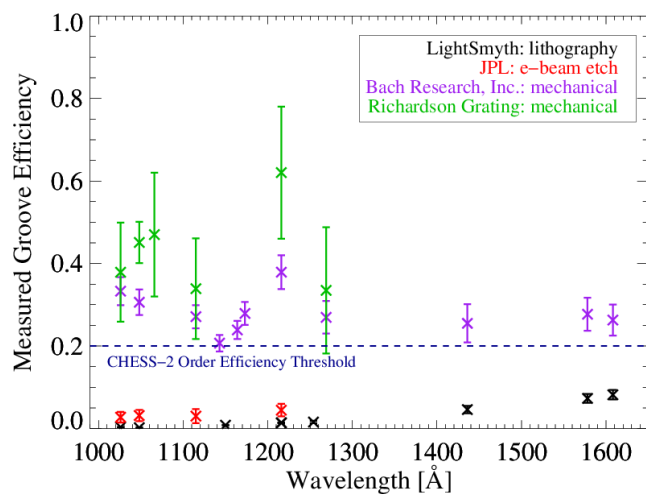


Fig. 3 A comparison of echelle gratings tested for use in the CHES instrument. We include the best-performing echelle gratings from the lithography etching R&D project undertaken by LightSmyth, Inc. (flown on CHES-1, 36.285 UG), the e-beam samples fabricated by JPL, and two mechanically-ruled replica gratings from Bach Research, Inc. and Richardson Gratings, respectively. Both mechanically-ruled gratings out-performed the R&D echelles and met the CHES minimum order efficiency threshold. Adapted from Hoadley et al. (2016).

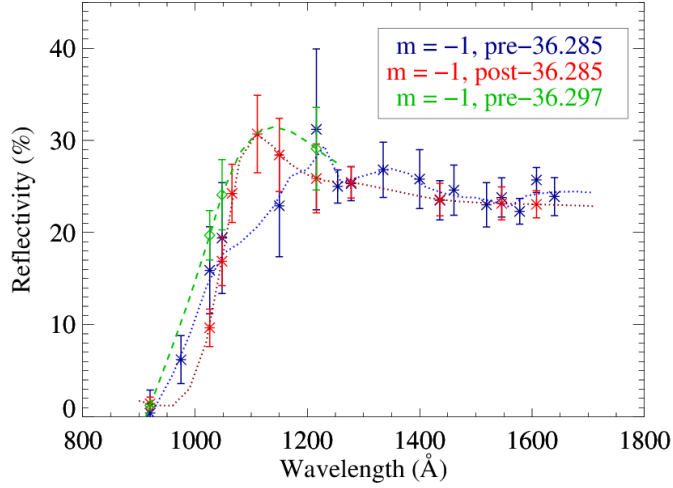


Fig. 4 The measured reflectivity (order efficiency \times reflectivity of Al+LiF) of the cross dispersing grating in CHESS over time, overplotted with simple spline curves to show the resemblance of each trial. The colored points and lines represent times before and after the CHESS-1 and CHESS-2 missions that the cross disperser grating efficiency was measured: pre-36.285 (blue) is before the cross disperser was installed and aligned into the instrument for the CHESS-1 flight, post-36.285 (red) is right after we recovered the instrument after the CHESS-1 flight and measured the post-flight efficiency of all the optical components, and pre-36.297 (green) is before the grating was installed and aligned into the instrument structure for the CHESS-2 flight. We focus on the reflectivity of the $m = -1$ order, which is the dispersion order used in the CHESS instrument. Because Al+LiF can exhibit efficiency degradations when not stored in a dry environment, we measure how the order reflectivity changes between CHESS-1 and CHESS-2 without re-coating the optic. No significant degradation of the coating has been measured between the first two flights of CHESS. Adapted from Hoadley et al. (2016).

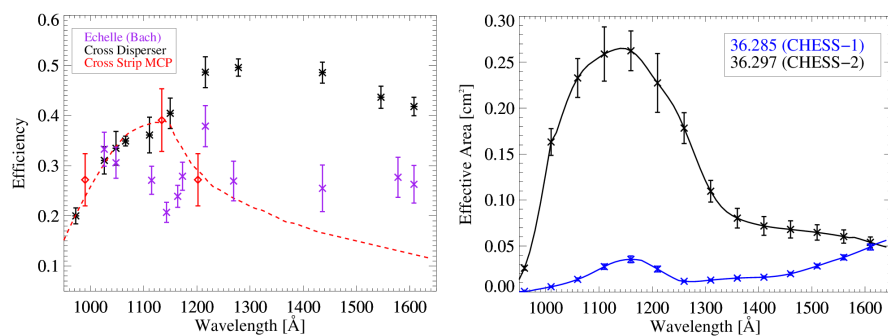


Fig. 5 *Left:* Performance (for each grating: peak order efficiency, and for the detector: detector quantum efficiency) of all optical components of CHES-2. For the first flight of CHES, the only component performance that changed significantly was the echelle efficiency, which was $\ll 0.1$ (10%) across the bandpass. *Right:* The CHES-2 effective area, including throughput loss from baffling, compared to the effective area of CHES-1. The total effective area of CHES-2 is about an order of magnitude larger than that of CHES-1, owing primarily to the large gain in echelle order efficiency across the bandpass. Adapted from Hoadley et al. (2016).

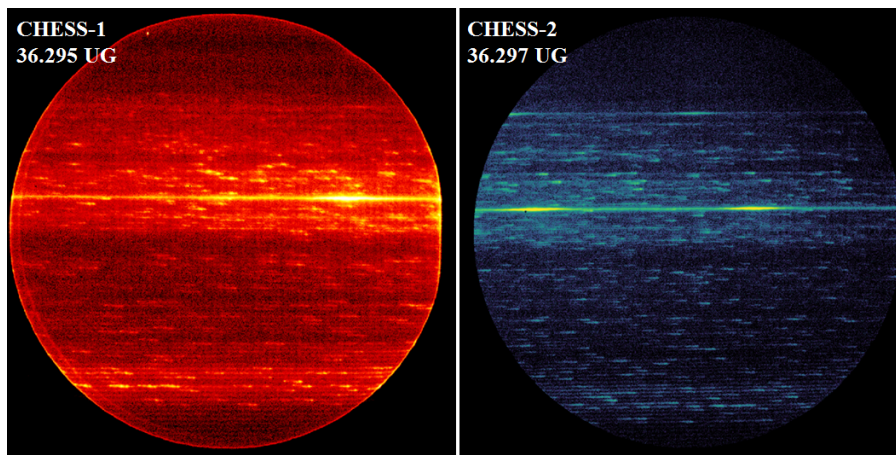


Fig. 6 Presented are the raw images of the CHESS-1 (left) and CHESS-2 (right; edge effects have been cropped out) echellograms from pre-flight calibrations (March 2014 and December 2015) using an arc lamp flowing 65%/35% H/Ar gas. The brightest feature in both images is H I-Ly α (λ 1215.67 Å); the CHESS-1 echellogram only shows Ly α in one echelle order, while the CHESS-2 echellogram disperses Ly α photons into two adjacent echelle orders. The other broad feature(s) visible in the CHESS-2 echellogram are H I-Ly β (1025.72 Å), about 1/4 of the way from the top of the image, and H I-Ly γ (97.25 Å), barely visible above the Ly β features. The more discrete features dotted throughout the spectrum are H₂ emission from electron-impact fluorescence. Adapted from Hoadley et al. (2014) and Hoadley et al. (2016).

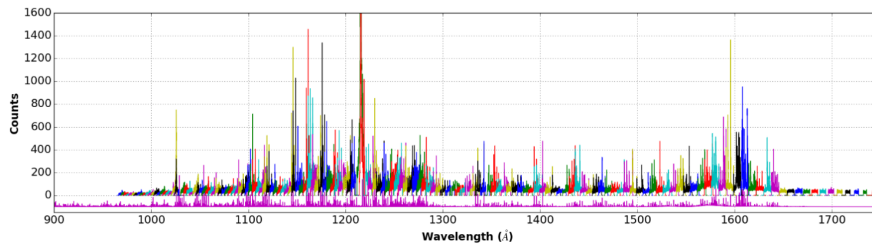


Fig. 7 The complete first-order wavelength solution for the pre-launch CHES-2 calibration spectra from $\lambda\lambda$ 900 - 1750 Å. The final wavelength solution was determined using H₂ fluorescence emission features and a functional extrapolation of the wavelength with a 6th-order polynomial fit. Over-plotted in magenta is the model H₂ fluorescence inside the arc lamp ($T_{eff} = 800$ K, $N(\text{H}_2) \sim 10^{19}$ cm⁻², $E_{electron} = 50$ eV). The spectrum is scaled to the highest total counts of the H₂ features; otherwise, Ly α would dominate the spectrum and the H₂ features would be washed out. To show how neighboring order spectra overlap and correlate to form the final 1D spectrum, individual order spectra have been plotted in different colors. Adapted from Hoadley et al. (2016).

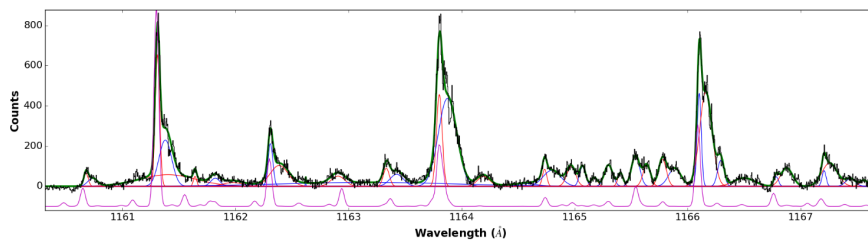


Fig. 8 The line spread function (LSF) fits of H₂ emission features in one order of the pre-launch calibration spectrum of CHES-2 (echelle order $m = 286$). The order spectrum is shown in black. Red and blue Gaussian line fits are shown for the narrow and broad Gaussian fits for each line, respectively. The green line is the sum of all Gaussian components to reproduce the spectrum. A modeled H₂ fluorescence spectrum is shown in magenta. Adapted from Hoadley et al. (2016).

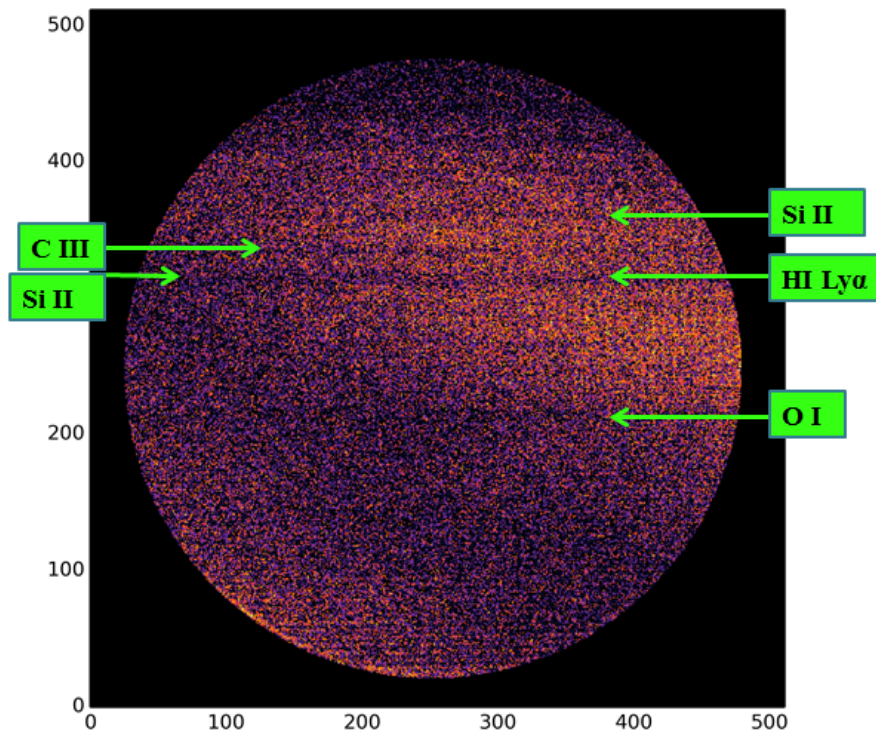


Fig. 9 The False-color representation of the flight echellogram from CHESS-1, taken on 24 May 2014, of α Vir. The purple/black regions represent areas with lower concentrations of photon counts, and blue/green pixels represent pixels with higher concentrations of photons collected. Marked with green arrows and labeled are the most prominent features in the echellogram. Because of the low S/N of the flight data, the echellogram has been binned to 512×512 , to show absorption features in the image. Adapted from Hoadley et al. (2014).

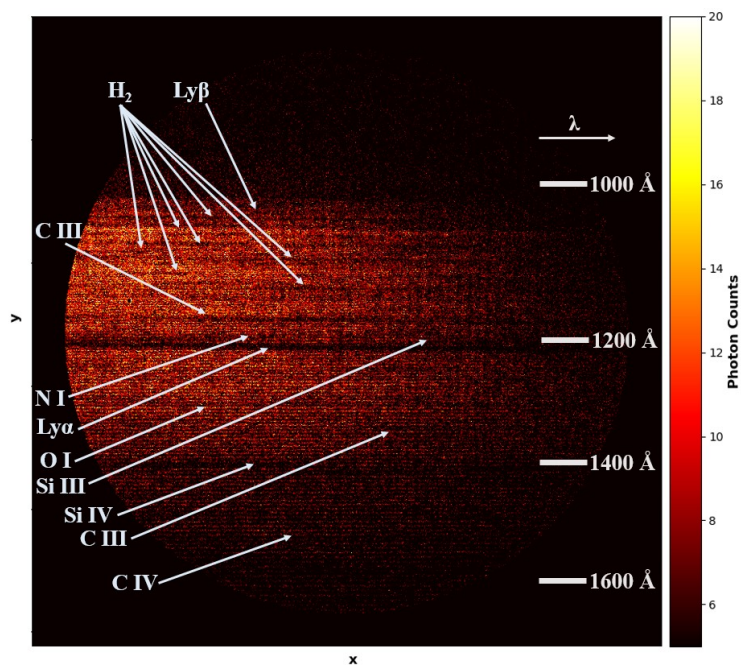


Fig. 10 The raw, false-color echellogram of ϵ Per, recorded over $t_{exp} \sim 250$ sec on NASA/CU mission 36.297 UG (CHESS-2). Along the right, we mark the rough wavelength coverage as a function of the detector y axis. In an individual echelle order, wavelength increases to the right. Stellar continuum through the far-UV acts as a back-light behind the interstellar material. Dark streaks in the continuum show stellar and interstellar atoms, ions, and molecules absorbing photons at specific wavelengths; prominent interstellar and stellar features are labeled with arrows pointing to the absorption lines and the absorption species along the left. Adapted from Hoadley et al. (2016).

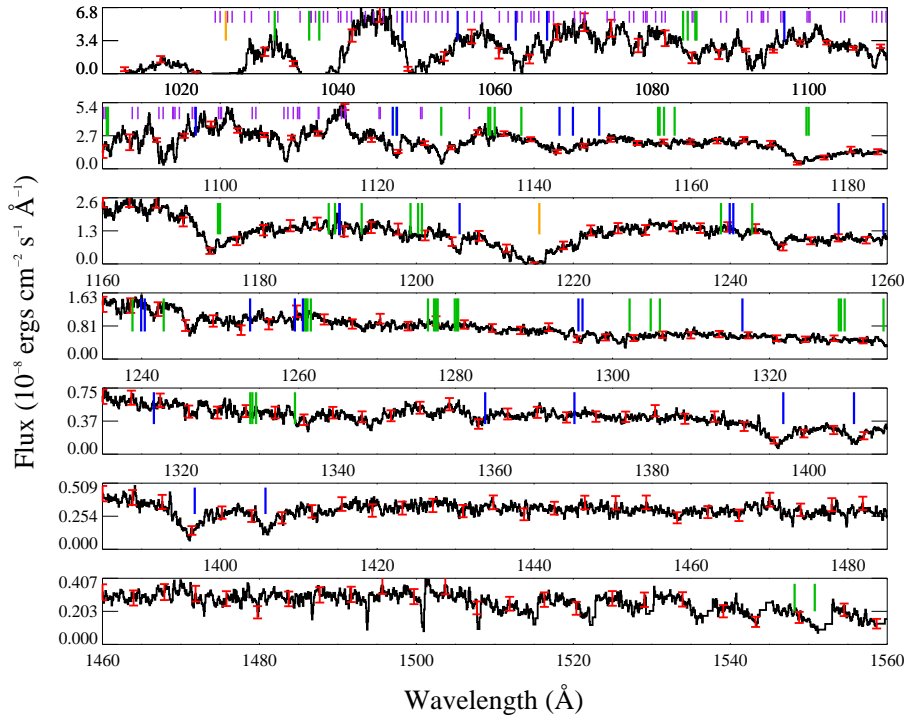


Fig. 11 The flux-calibrated CHES-2 spectra of ϵ Per from $\lambda = 1020 - 1550 \text{ \AA}$. Representative error bars are shown in red. The CHES-2 spectrum was flux-calibrated against *IUE* spectra of ϵ Per, and the continuum shape was compared with *Copernicus* spectra at $\lambda < 1150 \text{ \AA}$. Prominent stellar and interstellar absorption features are shown using vertical lines: purple lines show H_2 absorption features from $v = 0, J = 0 - 7$, orange lines show H I absorption, green lines show carbon, oxygen, and nitrogen species, and blue lines mark heavier metals (iron, silicon, sulfur, argon, magnesium, nickel, and copper).

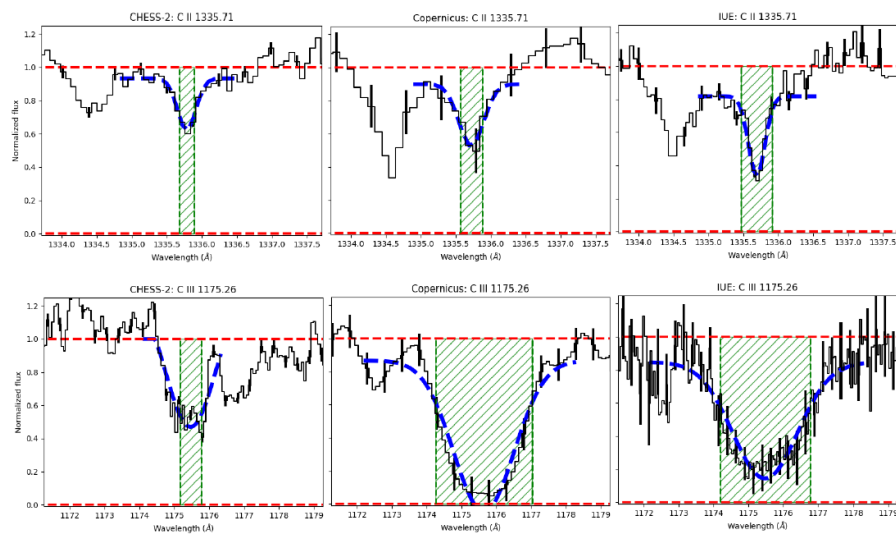


Fig. 12 (a) We present the normalized absorption features of different phases of interstellar carbon observed in the CHESS (left panels), Copernicus (middle panels), and *IUE* (right panels) FUV spectra of ϵ Per. We fit all lines with a Gaussian profile (blue dashed line) and determine the equivalent width (W_λ) from the area under the Gaussian (green hashed area). We determine W_λ for many metal lines found throughout the FUV in all data sets over a variety of interstellar phases - a comprehensive list of results is presented in Table 3.

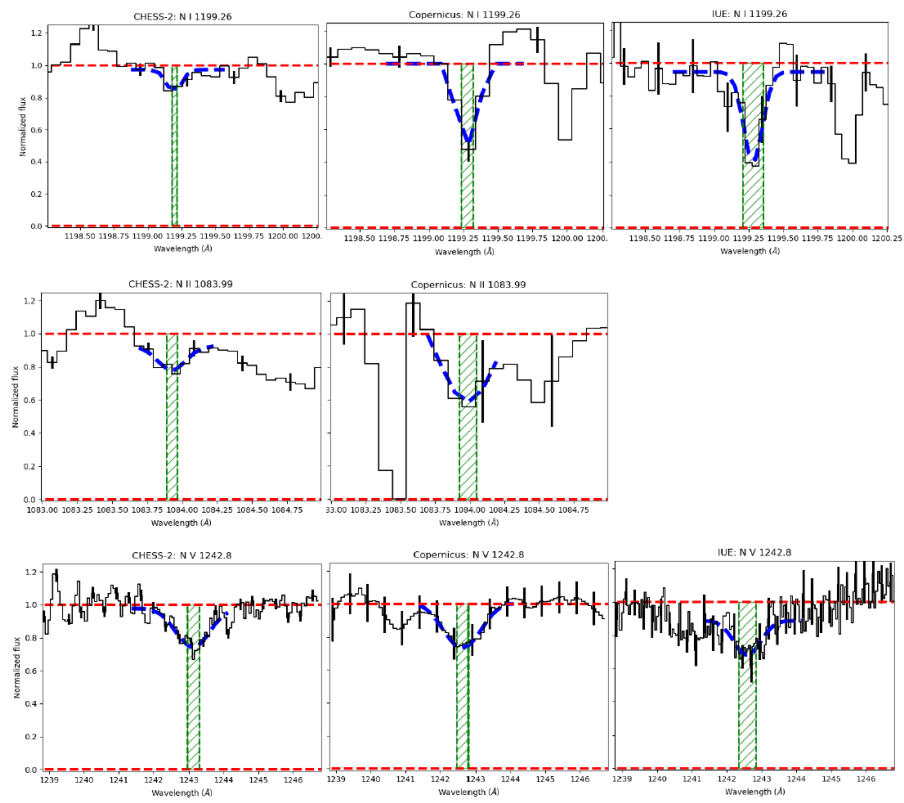


Fig. 12 (b) Continued; different phases of nitrogen observed by CHES, Copernicus, and *IUE*, their Gaussian fits (blue dashed line), and W_λ (green shaded area).

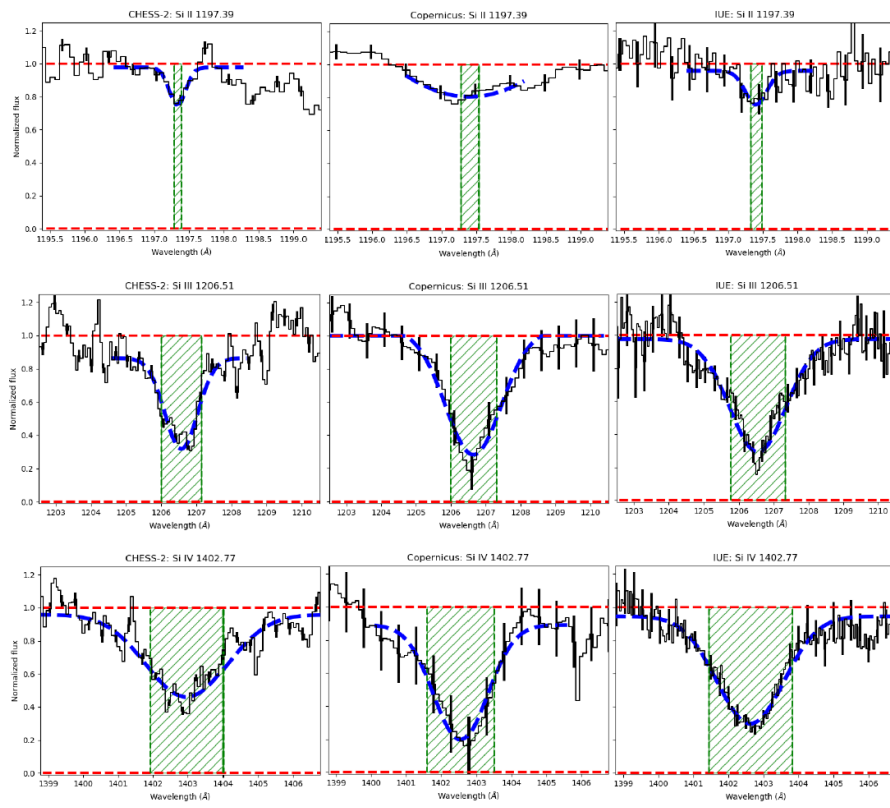


Fig. 12 (c) Continued; different phases of silicon observed by CHES, Copernicus, and *IUE*, their Gaussian fits (blue dashed line), and W_λ (green shaded area).

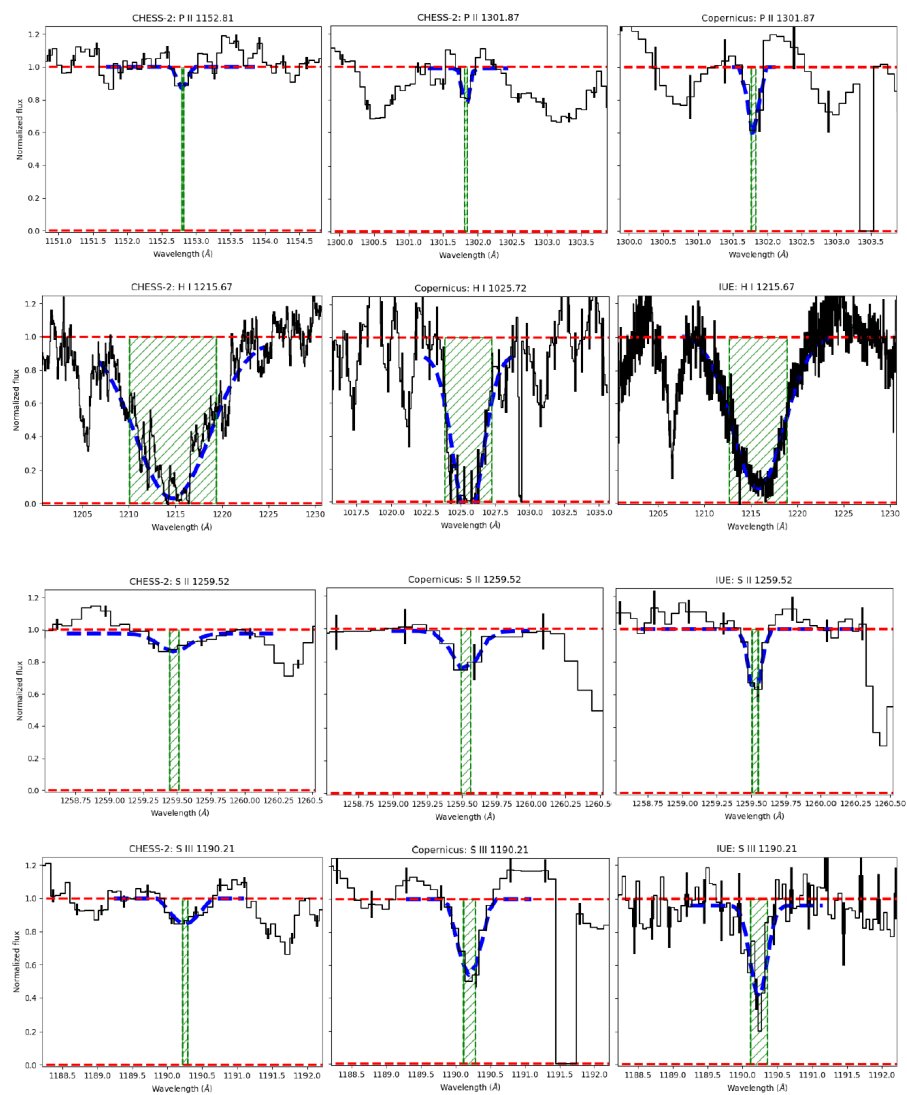


Fig. 12 (d) Continued; phosphorus, hydrogen, and sulfur observed by CHESS, Copernicus, and *IUE*, their Gaussian fits (blue dashed line), and W_λ (green shaded area).

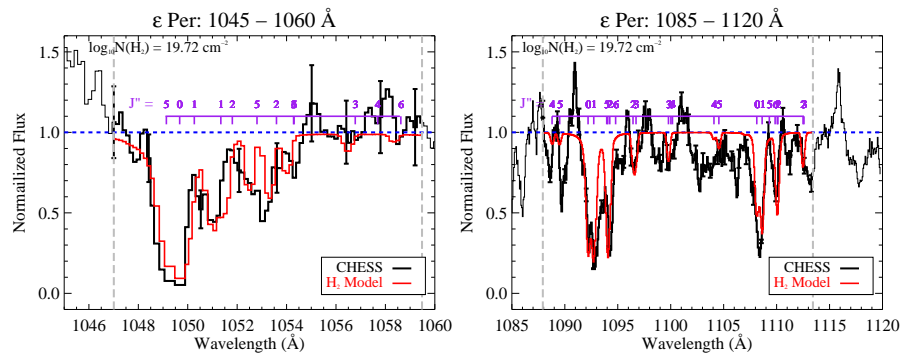


Fig. 13 Synthetic H₂ profile fits for the H₂(4 – 0) band (*left*) and H₂(1 – 0) and H₂(0 – 0) bands (*right*), shown in red, are overlaid on top of the ε Per spectrum. Molecular rotational levels are labeled with purple dashes. The best-fit Doppler velocities for all three spectral band fits is $b = 3.6 \text{ km s}^{-1}$.

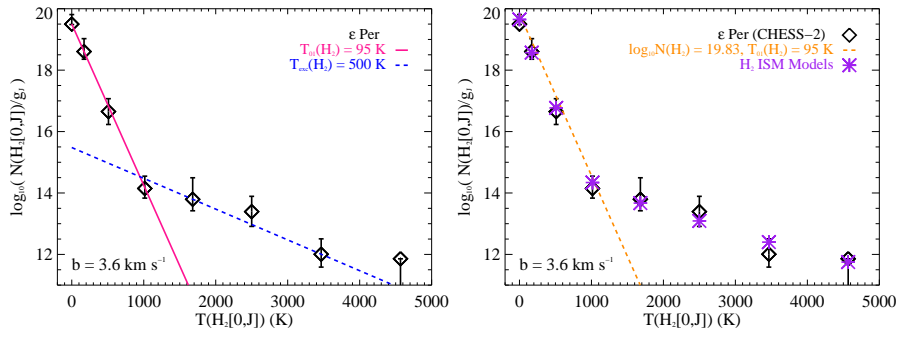


Fig. 14 We present the ϵ Per H_2 rotation diagram with two different model fits. *Left:* The H_2 rotation diagram is fit assuming the sightline has two temperature populations of H_2 : a cool, kinetic temperature, described by T_{01} (pink), and a warmer, “excitation” temperature, described by T_{exc} (blue). *Right:* The H_2 rotation diagram is fit with an H_2 equilibrium model (purple asterisks), which includes affects from UV-photon pumping, collisions with other particles, and formation/destruction rates of H_2 in a diffuse medium. The kinetic temperature derived from these models is shown in orange.